https://doi.org/10.5194/egusphere-2026-3290
Preprint. Discussion started: 24 August 2026

Characteristics and Mechanism of the Earthquake-Induced Sand Liquefaction in the January 7, 2025, Dingri M_W7.1 Earthquake

Zhichao Li[1, 2], Zhonghai Wu[1*], Shuai Han[1], Yang Gao[2, 3], Ting Huang[1, 2], Fuxin Fan[1, 4], Tingting Tian[1], Shiming Lu[1]

1) Institute of Geomechanics, Chinese Academy of Geological Sciences, Beijing 100081, China

2) School of Earth and Space Sciences, Peking University, Beijing 100871, China

3) Minnan Normal University, Zhangzhou 363000, China

4) School of Earth Sciences, China University of Geosciences (Wuhan), Wuhan, Hubei 430074, China

**Corresponding Author: Wu Zhonghai, E-mail: wuzhonghai8848@foxmail.com.*

Abstract

Sand liquefaction is a major secondary hazard following strong earthquakes, often causing lateral spreading, surface settlement, and sand volcanoes that lead to significant structural damage and economic losses. This study investigates sand liquefaction phenomena induced by the MW 7.1 Dingri earthquake in Tibet on January 7, 2025, aiming to reveal its spatial distribution and dynamic evolution. Using field surveys, drone imagery, remote sensing interpretation, and drilling data, the study identifies three main liquefaction zones: the southern Pengqu River valley, the area near Dingmu Co Lake, and the southeastern side of Kongmo Co Lake. Groundwater depths in the affected basin ranged from 5.6 to 9.0 meters, closely aligning with local river and lake water levels. Surface damage was dominated by lateral spreading and sand volcanoes. Field evidence and stress analysis suggest a multi-phase evolution: under tectonic stress and gravity, tensile fractures form;

https://doi.org/10.5194/egusphere-2026-3290
Preprint. Discussion started: 24 August 2026

seismic vibration triggers liquefaction, with pore fluid and sand being expelled through fractures. On gentle slopes, lateral spreading occurs as surface blocks slide and collide, generating additional fractures through compression, from which sand volcanoes erupt—often aligned linearly. This research offers critical insights into the mechanics of earthquake-induced sand liquefaction on the Tibetan Plateau and provides a foundation for future hazard assessment and mitigation efforts in seismically active, high-altitude regions.

Key words: Dingri MW 7.1 Earthquake; Earthquake-Induced Sand Liquefaction; Lateral Spreading; Sand volcano

1 Introduction

Earthquake-induced sand liquefaction is one of the most common and damaging secondary effects of strong ground shaking. Its surface manifestations, including sand venting, ground fissures, lateral spreading, and settlement, can cause severe damage to buildings, bridges, and lifelines, while also recording the near-surface response of sediments and pore fluids to seismic loading (Seed, 1968; Iwasaki, 1986; Ambraseys and Sarma, 1969; Xu et al., 2024; Liu et al., 2024; Xia et al., 2024). Because of these dual engineering and geological implications, liquefaction has long been a central topic in post-earthquake hazard investigation and interpretation (Dobry, 1989; Ishihara, 1993).

Previous studies have documented a wide range of liquefaction features and have shown that their occurrence is strongly influenced by groundwater conditions,

https://doi.org/10.5194/egusphere-2026-3290
Preprint. Discussion started: 24 August 2026

sedimentary environment, and local topography (Ambraseys and Sarma, 1969; Ishihara, 1993). In recent years, post-earthquake investigations have increasingly combined field observations with satellite imagery, UAV photogrammetry, and other remote-sensing approaches, making it possible to map liquefaction manifestations over large and inaccessible areas and to quantify local ground deformation with higher spatial continuity (Rathje and Franke, 2016). These advances have substantially improved our understanding of where liquefaction occurs and how it relates to geomorphic and hydrologic conditions.

However, compared with lowland alluvial plains and urban basin settings, liquefaction in high-altitude plateau basins remains less systematically described in terms of its internal deformation organization. Existing studies from the Pamir Plateau and the northern Tibetan Plateau have demonstrated that liquefaction can occur in cold and high-elevation environments and is closely related to shallow groundwater, sedimentary facies, and local topographic position (Yao et al., 2011; Wang et al., 2023). Yet, in many such cases, rear-edge tension cracks, frontal compressional ridges, and sand venting are still treated mainly as separate surface effects rather than as spatially linked components of a single lateral-spreading deformation system. This limits our understanding of how post-liquefaction surface response is organized within individual deformation units in plateau environments.

The 7 January 2025 Mw 7.1 Dingri earthquake in southern Tibet provides an important opportunity to address this problem. Recent studies have shown that this earthquake was a typical normal-faulting event associated with the Dingmu Co fault

https://doi.org/10.5194/egusphere-2026-3290
Preprint. Discussion started: 24 August 2026

in the western boundary zone of the Shenza-Dingjie rift, and that it triggered widespread secondary hazards, including sand liquefaction, in adjacent basin and valley settings (Xu et al., 2025; Li et al., 2025; Liu et al., 2025). In the affected area, liquefaction was not expressed simply by isolated sand volcanoes, but by recurrent combinations of rear-edge extensional deformation, frontal compressional ridges, and aligned clusters of sand venting. In this study, we integrate field surveys, UAV imagery, remote-sensing interpretation, and drilling data to investigate the spatial distribution of liquefaction triggered by the Dingri earthquake. Specifically, we aim to identify the principal liquefaction zones, define the geometry of lateral-spreading deformation units, and examine the spatial coupling among rear-edge extensional zones, frontal compressional ridges, and frontal sand-volcano belts. Rather than treating these features as independent earthquake effects, this study interprets them as different surface expressions of a coupled liquefaction–deformation system in a high-altitude fault-bounded basin setting.

2 Seismotectonic Setting

Due to the ongoing northeastward subduction of the Indian Plate, the Tibetan Plateau and its surrounding regions have consistently been among the most seismically active areas in China (Wu et al., 2015; Tian et al., 2023; Gao, 2024). On April 25, 2015, a magnitude 8.1 earthquake struck Nepal, followed by another magnitude 7.5 earthquake on May 12, 2015. The southern Tibetan region of China, located only about 40 km from the epicenter of the earthquake (Figure 2), experienced further seismic activity, with magnitude 5.4 and 5.7 earthquakes occurring on the

https://doi.org/10.5194/egusphere-2026-3290
Preprint. Discussion started: 24 August 2026

same day and the following day in the Nyalam and Dingri counties of the Southern Tibet Rift Zone (Wu et al., 2015). The close spatiotemporal correlation of these seismic events suggests a strong kinematic and dynamic link between the thrust faulting along the Himalayan Main Reverse Fault and the normal faulting within the Southern Tibet Rift Zone (Wu et al., 2015).

The 2025 MW 7.1 Dingri Earthquake occurred in the southern segment of the Dingjie-Shenza Rift Zone (Figure 1). This segment is characterized by three main Holocene-active faults, namely the Dingjie Fault, Guojia Fault, and Dingmu Co Fault, from east to west (Gao et al., 2024). The Dingmu Co Fault, a north-south trending normal fault with significant activity, triggered the earthquake. Historically, this fault has been the source of several earthquakes with magnitudes greater than 5.0 (Hou et al., 2020; Zhang et al., 2020; Tie et al., 2025). The epicenter of this earthquake was located in Dingri County, Shigatse, Tibet (28.50°N, 87.45°E), at a depth of 10 km. The focal mechanism solution indicates a predominantly normal faulting nature with a slight strike-slip component. The maximum intensity of the earthquake was IX (9), with the longest axis of the isoseismal lines trending nearly north-south, approximately 191 km in length and 152 km in width. The earthquake affected one city, six counties, and 45 towns in the Tibet Autonomous Region.

The strata in the earthquake area are relatively well-developed, with Paleozoic to Mesozoic strata exposed, the Triassic and Jurassic sedimentary rocks being the most widespread. The Cenozoic strata are mainly composed of Quaternary loose deposits (Figure 3), primarily found in the adjacent areas of the Pengqu River and its

https://doi.org/10.5194/egusphere-2026-3290
Preprint. Discussion started: 24 August 2026

tributaries (Jin, 2019; Tie et al., 2025). These deposits are mainly lacustrine, alluvial, and a small amount of fluvioglacial sediments from the Pleistocene and Holocene. The strata beneath the epicenter are primarily composed of Triassic and Jurassic limestones, shales, and sandstones, while both the northern and southern areas of the epicenter are underlain by Precambrian metamorphic rocks (Tie et al., 2025).

3. Methods

3.1. Post-earthquake field investigation and data sources

The earthquake-induced liquefaction features triggered by the 7 January 2025 Mw 7.1 Dingri earthquake were investigated through an integrated post-earthquake survey combining field observations, UAV imagery, pre- and post-earthquake satellite-image interpretation, and drilling information. The field investigation began on 9 January 2025, the third day after the earthquake, when surface liquefaction features and earthquake-induced ground deformation were still well preserved. The survey covered the entire area affected by macroseismic intensity IX, with particular attention to low-relief river valleys, lake margins, and basin-floor areas where liquefaction-related phenomena were visible.

A total of 180 field observation sites were investigated. At each site, we documented the occurrence, morphology, orientation, and spatial association of sand volcanoes, sand ejecta, ground fissures, lateral-spreading deformation, surface collapse, and compressional ridges. Site locations were recorded using the OMap positioning system, and field photographs and measurements were collected where

https://doi.org/10.5194/egusphere-2026-3290
Preprint. Discussion started: 24 August 2026

the features were accessible. Among the investigated sites, 10 relatively complete lateral-spreading deformation units were selected for morphometric comparison and exploratory statistical analysis. These 10 units were selected because they showed clear and mappable combinations of rear-edge extensional deformation, frontal compressional deformation, and associated sand venting.

Pre- and post-earthquake satellite images were compared to identify newly formed liquefaction features and to distinguish earthquake-induced sand ejecta from pre-existing surface textures. The pre-earthquake image was a GF-7 image acquired on 27 December 2024, and the post-earthquake image was a Tianditu image acquired on 15 January 2025. Both images were accessed and interpreted using the 91 Weitu platform. These images were used to identify the spatial distribution of sand-volcano fields, sand-ejecta patches, surface collapse zones, and other liquefaction-related disturbances. Image interpretation was checked against field observations to reduce misclassification caused by pre-existing landforms, human disturbance, or non-seismic surface processes.

UAV surveys were carried out at representative liquefaction sites using a DJI Phantom 4 Pro. The flight height was approximately 150 m. UAV photographs were processed using Pix4D software to generate high-resolution orthomosaics and to assist in the interpretation of local deformation structures. The UAV-derived products were mainly used to verify the geometry and spatial relationships of deformation elements, including rear-edge cracks, disturbed ground, frontal ridges, and aligned sand vents.

Drilling and hydrogeological information were used to constrain the shallow sedimentary structure and groundwater conditions in the affected basin areas. These data provided supporting evidence for the presence of saturated sandy or silty layers and helped evaluate the relationship between liquefaction occurrence and shallow groundwater conditions. Because groundwater depth may vary seasonally and may have changed after the earthquake, groundwater information was used as an approximate constraint on the hydrogeological setting rather than as an exact representation of coseismic groundwater level.

3.2. Identification of liquefaction zones and lateral-spreading deformation units

Liquefaction zones were identified by combining field evidence with pre- and post-earthquake image interpretation. In this study, a liquefaction zone refers to a cluster of earthquake-induced liquefaction features developed within the same geomorphic setting, such as a river valley, lake margin, or low-relief basin floor. Diagnostic features included sand volcanoes, sand ejecta, water-escape traces, ground fissures, surface collapse, lateral-spreading deformation, and compressional ridges.

A surface feature was interpreted as earthquake-induced liquefaction when it satisfied the following conditions: (1) sand or silty-sand ejecta was visible at the ground surface; (2) the feature appeared after the earthquake in comparison with pre-earthquake imagery; (3) it was spatially associated with fresh ground cracks, collapse zones, lateral spreading, or compressional deformation; and (4) it occurred in a geomorphic setting favorable for shallow saturated sandy deposits. Features with unclear origin, strong human disturbance, obvious fluvial reworking, or insufficient field evidence were not used in the morphometric analysis.

https://doi.org/10.5194/egusphere-2026-3290
Preprint. Discussion started: 24 August 2026

Because sand volcanoes in the study area commonly occurred as aligned clusters and were spatially associated with rear-edge extensional deformation and frontal compressional ridges, the analysis was conducted at the scale of lateral-spreading deformation units rather than at isolated sand-vent points. A lateral-spreading deformation unit was defined as a mappable ground-failure body containing, where preserved, four geomorphic elements: (1) a rear-edge extensional zone marked by cracks, collapse, or minor scarps; (2) lateral margins bounding the disturbed ground; (3) a frontal compressional ridge or compressional deformation zone; and (4) an associated frontal or marginal sand-volcano belt.

In this framework, rear-edge extension, frontal compression, lateral spreading, and sand venting were treated as spatially linked surface expressions of the same liquefaction-related deformation system. Only deformation units with sufficiently clear boundaries and internally consistent deformation patterns were included in the quantitative comparison. Incomplete or ambiguous cases were documented qualitatively but excluded from the statistical analysis.

3.3. Morphometric characterization of deformation units

To compare the geomorphic expression of different lateral-spreading deformation units, three simplified morphometric parameters were measured: rear-edge extensional-zone width, frontal compressional-ridge height, and apparent sand-volcano area. These parameters were selected because they represent three key components of the inferred liquefaction–deformation system: rear-edge extension, frontal compression, and sand-water expulsion.

https://doi.org/10.5194/egusphere-2026-3290
Preprint. Discussion started: 24 August 2026

The width of the rear-edge extensional zone was measured from post-earthquake images using the 91 Weitu platform. It was defined as the horizontal width of the visually identifiable collapse or extensional deformation zone at the rear part of a lateral-spreading unit. The measurement was made across the zone affected by cracks, collapse, or disturbed ground, rather than along a single fracture. This parameter was used to characterize the scale of rear-edge extension within each deformation unit.

The height of the frontal compressional ridge was measured directly in the field. It was defined as the vertical relief between the crest of the compressional ridge and the adjacent ground surface. Where the ridge morphology varied along strike, representative measurements were taken from the most continuous and clearly preserved ridge segment. This parameter was used to describe the degree of frontal compression associated with lateral spreading.

The scale of sand venting was characterized by the apparent surface area of sand-volcano and sand-ejecta deposits. Sand-volcano areas were identified by comparing the 27 December 2024 pre-earthquake GF-7 image with the 15 January 2025 post-earthquake Tianditu image. Newly appeared light-toned or texturally distinct sand-ejecta patches were delineated manually using the 91 Weitu platform. The mapped polygons were then summed to obtain the total apparent sand-volcano area for each deformation unit. Field observations were used to verify the interpretation where accessible.

The sand-volcano area represents the visible surface footprint of sand ejecta at the time of image acquisition and field investigation. It does not represent the true

https://doi.org/10.5194/egusphere-2026-3290
Preprint. Discussion started: 24 August 2026

erupted volume of liquefied material. Similarly, extensional-zone width and compressional-ridge height were treated as comparative morphometric indicators rather than standardized liquefaction severity indices. Their purpose was to describe the relative organization of rear-edge extension, frontal compression, and sand venting among the mapped deformation units.

3.4. Exploratory comparison among deformation units

The morphometric comparison was based on the 10 deformation units that were clearly identifiable in both field observations and remote-sensing interpretation. For each unit, rear-edge extensional-zone width, frontal compressional-ridge height, and apparent sand-volcano area were compiled into a comparative dataset.

To examine the relative variation among these parameters, the measured values were normalized using min–max scaling before plotting. Scatter plots were used to compare pairwise relationships among extensional-zone width, compressional-ridge height, and sand-volcano area. Pearson correlation coefficients were calculated to assess possible linear relationships, and Spearman rank correlation coefficients were additionally calculated to evaluate monotonic trends.

Because the number of deformation units is limited, the statistical analysis was treated as exploratory rather than predictive. The purpose was not to establish a statistically robust model of liquefaction intensity, but to evaluate whether rear-edge extension, frontal compression, and sand venting show coherent variation within the mapped deformation units. Therefore, the correlation results were interpreted together with field observations, image interpretation, and the mapped spatial arrangement of

https://doi.org/10.5194/egusphere-2026-3290
Preprint. Discussion started: 24 August 2026

deformation elements.

3.5. Uncertainty and limitations

Several sources of uncertainty may affect the mapping and morphometric comparison. First, field investigation began on the third day after the earthquake, when most deformation features were still fresh, but some small sand vents, cracks, or sand-ejecta margins may already have been modified by wind, freeze–thaw processes, surface runoff, human activity, or local reworking. Therefore, the mapped distribution may underestimate the original extent of liquefaction features.

Second, the identification of sand-volcano areas was based on comparison between pre- and post-earthquake images acquired on 27 December 2024 and 15 January 2025. Although this comparison is useful for detecting newly formed sand-ejecta patches, some small or low-contrast features may not be visible in the satellite images. Conversely, some bright-toned surface patches may be difficult to distinguish from non-liquefaction materials without field verification. To reduce this uncertainty, remote-sensing interpretation was checked against field observations wherever possible.

Third, the rear-edge extensional-zone width was measured from post-earthquake imagery as the visually identifiable width of the collapse or disturbed zone. This parameter may be affected by image resolution, surface contrast, and the subjective delineation of deformation boundaries. Therefore, it should be interpreted as a relative measure of deformation scale rather than an exact geotechnical parameter.

Fourth, the frontal compressional-ridge height was measured in the field, but

https://doi.org/10.5194/egusphere-2026-3290
Preprint. Discussion started: 24 August 2026

ridge morphology may vary along strike and may be locally modified by collapse or surface disturbance. The selected measurements therefore represent the best-preserved or most representative ridge segments within each deformation unit.

Fifth, the apparent sand-volcano area was mapped as a surface footprint and cannot be directly converted into sand-ejecta volume. The mapped area may underestimate the original venting area where ejecta were eroded, covered, or mixed with surrounding surface materials. It may also overrepresent venting intensity where thin sand sheets spread widely over the ground surface.

Finally, the statistical comparison was based on only 10 deformation units. The Pearson and Spearman correlation coefficients were therefore used only to explore possible relationships among deformation parameters. They were not used to establish a predictive model or to infer statistically robust regional liquefaction laws.

4 Regional deformation background and study-area selection

4.1 Coseismic surface deformation pattern of the Dingri earthquake

The coseismic surface deformation associated with the Dingri earthquake extended from the southern part of Cuoguo Township to the northern part of Yammu Dingco over a distance of approximately 36.5 km (Shao et al., 2025). The width of the deformation zone varies markedly, ranging from tens of meters to several kilometers.

According to deformation style and intensity, the coseismic deformation belt can be divided into northern and southern sections. In the northern section, deformation is relatively concentrated and intense, especially north of the Changsuola Reservoir,

https://doi.org/10.5194/egusphere-2026-3290
Preprint. Discussion started: 24 August 2026

where vertical displacement locally reaches up to 3 m (Shao et al., 2025). In contrast, the southern section, including the Pengqu River valley and the eastern shore of Dingmu Co Lake, is characterized by more diffuse deformation distributed across unconsolidated sediments. In the Pengqu River area, the diffuse deformation zone on the northern bank reaches a maximum width of about 6.5 km. Compared with the northern section, the southern section exhibits more typical ground deformation developed in loose surficial deposits, providing favorable conditions for liquefaction-related lateral spreading.

4.2 Selection of the key liquefaction study areas

This study focuses on sand liquefaction developed in the Dingmu Co Basin, where strong shaking and widespread unconsolidated Quaternary sediments favored the development of liquefaction and lateral spreading (Figures 2, 3). Within this basin, two representative areas were selected for detailed investigation: the eastern shore of Dingmu Co Lake and the Pengqu River valley.

These two areas were selected for three reasons. First, both are located in the zone of strong shaking and exhibit clear evidence of earthquake-induced sand liquefaction. Second, both areas preserve well-developed combinations of sand venting, extensional cracks, compressional ridges, and lateral spreading, making them suitable for identifying representative lateral-spreading deformation units. Third, although the two areas differ in geomorphic setting, one being associated mainly with alluvial-fan and lakeshore deposits and the other with floodplain and riverbank deposits, they both show a similar deformation organization characterized by

https://doi.org/10.5194/egusphere-2026-3290
Preprint. Discussion started: 24 August 2026

rear-edge extension and frontal compression. This makes them ideal for comparing the geometry and internal structure of liquefaction-related deformation units in different sedimentary environments.

Accordingly, the following sections focus on the spatial distribution of liquefaction in the Dingmu Co Basin and on the geometry, internal characteristics, and development of representative lateral-spreading deformation units in these two key areas.

5 Spatial Distribution of sand liquefaction and Identification of Representative Deformation Units

The liquefaction points triggered by this earthquake are primarily distributed across the Dingmu Co Basin, the Pengqu River segment of the Dingmu Co Basin, the Pengqu River segment of the Guojia Basin, and the Kuanhe Valley segment of the YeruZangbu River in the Dingjie Basin (Xu et al., 2025). This study focuses specifically on the sand liquefaction developed within the Dingmu Co Basin, where the surface intensity reached IX and strong ground shaking produced widespread liquefaction-related deformation (Figures 2, 3).

Field surveys, combined with remote sensing interpretation, identified 180 sand liquefaction points triggered by the earthquake within the Dingmu Co Basin (Figure 6). These liquefaction points are distributed in a linear pattern along the fault zone, occurring in the southern Pengqu River Valley, the eastern shore of Dingmu Co Lake in the central region, and the southeastern side of Kongmo Co in the northern part. Based on the spatial association among rear-edge extensional deformation, frontal

https://doi.org/10.5194/egusphere-2026-3290
Preprint. Discussion started: 24 August 2026

compressional ridges,and sand venting, two representative types of liquefaction-related lateral-spreading deformation units can be identified. One type is represented by the liquefaction zone along the eastern shore of Dingmu Co Lake, where sand volcanoes form along tension fractures at the front edge of the alluvial fan, large compressional ridge develop in the central to frontal part of the fan, extensional deformation zones occur in the middle of the fan, and fault scarps are present at the top of the fan under the control of fault activity. Primary coseismic fault scarps were distinguished from liquefaction-related cracks and were not treated as part of the morphometric deformation units unless they showed direct spatial coupling with sand venting and lateral spreading. The other type occurs in the Pengqu River Valley, where sand volcanoes develop along tension fractures on the high river floodplain, smaller compressional ridge occur toward the rear of the floodplain, and extensional deformation zones develop along the riverbank slopes (Figure 5).

The surface manifestations of liquefaction in the Dingmu Co Basin include spray features, sand volcanoes, tension fractures, extensional deformation zones, and compressional ridges. venting points are primarily found near the top of the alluvial fan on the eastern shore of Dingmu Co Lake and the northeast shore of Nixia Co to the north. Due to the cold climate in the seismic area, these venting points often form multiple layers of ice, suggesting that multiple liquefaction events may have occurred during this earthquake. A series of north-south oriented venting points can be observed along fault scarps at the top of the alluvial fan on the eastern shore of Dingmu Co Lake (Figure 4b), indicating a possible association with seismic activity

https://doi.org/10.5194/egusphere-2026-3290
Preprint. Discussion started: 24 August 2026

along the north-south trending Dingmu Co Fault.

Sand volcanoes form when seismic or vibrational forces cause liquefaction of saturated sandy layers, which then expel the liquefied sand through surface fractures or weak points and accumulate on the surface, creating dune-like deposits. Laterally, sand volcanoes are primarily located near the edge of the alluvial fan, where compressional ridge are present (Figures 4c, 5a, c, 7). Longitudinally, they are mainly found in the Pengqu River Valley and along the eastern shore of Dingmu Co Lake (Figure 4). Some sand volcanoes also develop along the northern segment of the Dingmu Co Fault (Figures 3, 6a). A series of sand volcanoes can be observed developing along tension fractures in the Pengqu River Valley, east of the Gading Line, and on the eastern shore of Dingmu Co Lake. These observations indicate that sand venting in the study area is not expressed simply as isolated points, but commonly occurs as aligned clusters spatially associated with lateral-spreading deformation.

5.1 Representative deformation units on the eastern shore of Dingmu Co Lake

Intense liquefaction-induced deformation developed along the eastern shore of Dingmu Co Lake. In this area, the liquefaction-related deformation can be organized into representative lateral-spreading deformation units composed of rear-edge extensional deformation, frontal compressional ridges, and frontal sand venting. This deformation is manifested in several forms: sand volcanoes along east-west trending tension fractures at the front edge of the alluvial fan, large compressional ridge in the central part of the alluvial fan, and north-south trending extensional deformation

https://doi.org/10.5194/egusphere-2026-3290
Preprint. Discussion started: 24 August 2026

zones in the middle of the fan. At the top of the alluvial fan, fault activity controls the development of fault scarps. The liquefied sand volcanoes generated by this earthquake are generally light gray-yellow in color, predominantly exhibiting well-preserved round shapes, with some fan-shaped forms. The radii of these sand volcanoes range from 0.1 m to 1.5 m, and their heights range from 0.1 m to 0.3 m (Figures 5, 7). The core of the sand volcanoes tends to have a coarser grain size and is typically rounded or elongated, with finer grains at the edges that radiate outward.

Through detailed field investigations, this study identifies two types of sand volcanoes. One type occurs randomly, without showing a clear linear pattern, and the cores of these sand volcanoes are more rounded and well formed. The other type is primarily found along tension fractures near the compressional ridge, where the cores of the sand volcanoes are elongated. In this case, the cores of a series of sand volcanoes are connected, presenting a distinct linear arrangement. By statistically analyzing the orientations of tension fractures associated with sand volcanoes (Figures 6b, 8a, d, e, 11c), it was found that the dominant orientations of most tension fractures can be divided into two groups: one group is near east-west, perpendicular to the compressional ridge at the edge of the alluvial fan, and the other group is near north-south, nearly parallel to the compressional ridge. These two groups of tension fractures are often accompanied by well-formed linear sand volcanoes. Notably, the tension fractures at the rear edge tend to be larger in scale, with corresponding compressional ridge also larger, reaching a maximum size of 76 cm. These features together suggest that the eastern shore of Dingmu Co Lake preserves a

https://doi.org/10.5194/egusphere-2026-3290
Preprint. Discussion started: 24 August 2026

well-developed deformation-unit structure in which rear-edge extension, frontal compression, and sand venting are spatially coupled.

5.2 Representative deformation units along the Pengqu River

Intense liquefaction-induced deformation also occurred on the Pengqu Riverbed and in the lower terraces during this earthquake (Xu et al., 2025). Similar to the eastern shore of Dingmu Co Lake, the Pengqu River area also exhibits representative lateral-spreading deformation units, although their scale and orientation differ. Sand volcanoes developed on the high river floodplain along the Pengqu River, expelling material along tension fractures (Figures 5a, c). These sand volcanoes are large, with diameters reaching up to 4 m and heights up to 40 cm. At the rear edge of the floodplain, small-scale compressional ridge developed in a near north-west orientation (Figure 8a, b; Figures 9c, e), with heights ranging from 5 to 10 cm. Extensional deformation zones also developed along the riverbank slopes, with scarp offsets ranging from 20 to 50 cm (Figures 5b, 8b).

Statistical analysis of the orientations of tension fractures (Figures 9c, e) revealed that these fractures can be classified into two main types: north-west trending and north-east trending. Sand volcanoes developed along both types of tension fractures, with the north-west trending fractures predominating, and the sand volcanoes associated with these fractures being larger in scale. In contrast, the sand volcanoes associated with the north-east trending fractures are smaller in size. Compared with the eastern shore of Dingmu Co Lake, the Pengqu River deformation units show smaller compressional ridges and narrower extensional deformation zones, but the

https://doi.org/10.5194/egusphere-2026-3290
Preprint. Discussion started: 24 August 2026

same basic organization of rear-edge extension, frontal compression, and aligned sand venting can still be recognized.

6 Controls on the Occurrence and Distribution of sand liquefaction

The occurrence and spatial distribution of sand liquefaction in the Dingri earthquake were controlled by the combined effects of strong ground shaking, favorable sedimentary conditions, and shallow groundwater. Rather than discussing these factors in a general sense, this section focuses on how they help explain the concentration of liquefaction in the Dingmu Co Basin and the development of representative lateral-spreading deformation units in the eastern shore of Dingmu Co Lake and the Pengqu River valley.

6.1 Ground shaking

In the Dingri earthquake, intense ground shaking provided the direct triggering condition for sand liquefaction and the associated surface deformation. The maximum seismic intensity reached IX in the main affected area (Figures 2, 3), and the liquefaction sites analyzed in this study are mainly located within the strong-shaking zone. Instrumental records show that the peak ground acceleration at station D007, located 67 km from the epicenter, reached 0.4g (Figures 10b–d). Such strong shaking would have promoted rapid rearrangement of loose sandy sediments, reduction of pore volume, and sharp increases in excess pore-water pressure, thereby creating favorable conditions for liquefaction and lateral spreading (Liu et al., 2017; Zhuang et al., 2025).

https://doi.org/10.5194/egusphere-2026-3290
Preprint. Discussion started: 24 August 2026

Frequent aftershocks may also have contributed to repeated liquefaction or continued deformation after the main shock (Huang and Yu, 2013). Previous studies have shown that once the original soil structure is disrupted by initial liquefaction, the liquefied layer may become more unstable and more susceptible to re-liquefaction if excess pore-water pressure is not fully dissipated before subsequent shaking (Ha et al., 2011; Youd, 1973, 2003). In the Dingri earthquake sequence, aftershocks were numerous. As of 10:00 on January 20, a total of 5396 aftershocks had been recorded near the epicenter, including 12 events with magnitudes greater than 4.0 and a maximum aftershock magnitude of 5.0 (Figure 10a; Yao et al., 2025). This high aftershock frequency may help explain the persistence of sand venting and the repeated development of liquefaction-related surface features observed in the study area.

6.2 Sedimentary setting

Previous studies have shown that sediment type is one of the key factors controlling the susceptibility and intensity of sand liquefaction (Youd, 2003). In the Dingri earthquake area, liquefaction developed mainly within loose Quaternary sediments. The principal Quaternary deposits include Holocene swamp deposits, alluvial deposits, residual materials, and Pleistocene glacial and lacustrine deposits (Tie et al., 2025). Previous research indicates that recently deposited, weakly consolidated granular sediments are generally more prone to liquefaction than older or better-cemented deposits (Youd, 1973, 2003). Holocene sediments are therefore more susceptible than Pleistocene deposits, and well-sorted sandy materials are typically more liquefiable than poorly sorted residual soils or moraine deposits.

In the present study area, the main liquefaction zones are concentrated in basin- and valley-floor settings dominated by Quaternary loose sediments, especially around the banks of Dingmu Co Lake and the Pengqu River valley (Figure 3). These sediments mainly include Holocene aeolian sands, fluvial sands, and ancient lacustrine sandy deposits, all of which provide favorable material conditions for liquefaction. The concentration of liquefaction in these river–lake margin settings indicates that sedimentary environment played an important role not only in the occurrence of liquefaction, but also in the development of laterally spreading deformation units.

6.3 Groundwater conditions

Groundwater in the region can be divided into two main types: Quaternary pore water and bedrock fracture water (Jin et al., 2019). Quaternary pore water is mainly distributed in river-valley areas and is hosted by alluvial and colluvial sand and gravel deposits. It is primarily replenished by atmospheric precipitation and meltwater from high mountain glaciers and is discharged downstream or into rivers. Bedrock fracture water is mainly stored in weathered and fractured bedrock zones, where water content and permeability are spatially variable and generally lower than those of pore-water-bearing sediments. This fracture water is also recharged by precipitation and mountain meltwater and commonly discharges into valleys, mountain-front alluvial deposits, and river channels (Jin et al., 2019).

https://doi.org/10.5194/egusphere-2026-3290
Preprint. Discussion started: 24 August 2026

To better constrain groundwater conditions in the study area, eight boreholes were drilled along the terraces of the Pengqu River and the shores of Dingmu Co Lake (Figure 11). These boreholes span the IX, VIII, and VII intensity zones (Figure 10b). Boreholes BDMC2QZ-4 (H4161 m) and BDMC2QZ-2 (H4160 m) show similar groundwater conditions (Figure 11a), with groundwater depths ranging from 5.6 to 6.7 m and water levels between H4154.3 m and H4154.4 m. Nearby borehole BDMC2KQZ-4 (H4173 m) records a groundwater depth of 8.4 m and a water level of H4164.6 m. Further east, boreholes BPQ9TQZ-7-1 (H4162 m) and BPQ9TQZ-3-1 (H4169 m) along the Pengqu River indicate groundwater depths of 6.2 m and 9.0 m, with corresponding water levels of H4155.8 m and H4160 m, respectively. These five boreholes together indicate that the typical groundwater depth in the main liquefaction belt is relatively stable, generally ranging from 5.6 to 9.0 m.

Further east, on the eastern side of the Guojia Fault, boreholes BPQ12TQZ-6 (H4187 m), BPQ12TQZ-14 (H4177 m), and BPQ12TQZ-18 (H4200 m) record groundwater depths of 24.8 m, 0.2 m, and 18.4 m, respectively (Figure 11a). Angular gravels were encountered in these boreholes, suggesting that fault activity may have influenced local groundwater conditions. Because groundwater levels east of the Guojia Fault are strongly affected by local structural conditions, the five boreholes west of the fault are considered more representative of the typical hydrogeologic setting of the main liquefaction zone.

The borehole data show that the groundwater level in the main study area is broadly comparable to the water levels of the Pengqu River and Dingmu Co Lake.

https://doi.org/10.5194/egusphere-2026-3290
Preprint. Discussion started: 24 August 2026

This indicates that river and lakeshore environments helped maintain shallow saturated sandy layers, thereby providing favorable hydrogeologic conditions for earthquake-induced liquefaction. In combination with loose Quaternary sandy deposits, this shallow groundwater setting strongly favored both liquefaction occurrence and the development of sand venting and lateral spreading in the Dingmu Co Basin.

6.4 Integrated controls on the development of deformation units

Taken together, the data indicate that the concentration of liquefaction in the Dingmu Co Basin and the formation of representative lateral-spreading deformation units were not controlled by a single factor. Instead, they resulted from the joint action of strong seismic loading, loose Quaternary sandy sediments, and shallow groundwater conditions. Strong shaking provided the direct triggering mechanism, sandy sediments supplied the liquefiable material, and shallow groundwater maintained the saturated state required for pore-pressure build-up. Under these combined conditions, the basin margin and river–lake fringe environments became favorable sites not only for liquefaction occurrence, but also for the development of rear-edge extension, frontal compression, and aligned sand venting within the same deformation system.

7 Discussion

7.1 Unit-based interpretation of liquefaction-related surface deformation

As described above, liquefaction with different deformation characteristics

https://doi.org/10.5194/egusphere-2026-3290
Preprint. Discussion started: 24 August 2026

developed along the eastern shore of Dingmu Co Lake and on both banks of the Pengqu River. Although these two areas differ in geomorphic setting and deformation scale, they share a common structural organization. In both areas, the most typical liquefaction-related surface response is not an isolated sand volcano or an isolated fissure, but a lateral-spreading deformation unit composed of rear-edge extensional deformation, frontal compressional ridges, and aligned sand venting.

On the eastern shore of Dingmu Co Lake, most sand volcanoes developed along tension fractures and show distinct linear arrangements. Two dominant fracture sets can be recognized: one set trends approximately north-south and is broadly parallel to the compressional ridges, whereas the other set trends approximately east-west and is largely perpendicular to them. Both fracture sets are associated with linearly distributed sand volcanoes. In some locations, east-west trending sand-volcano alignments cut across north-south trending ones and across the compressional ridges (Figures 6c, d), may suggest that sand venting and surface deformation evolved dynamically rather than being produced in a single instantaneous event.

A similar relationship is observed in the valley west of the Gading Line highway (Figures 7c, d). At Observation Point 24, sand volcanoes developed along north-south oriented fractures are partially covered by compressional ridges and therefore preserved only as incomplete semi-circular or fan-shaped forms. In contrast, sand volcanoes developed along east-west oriented fractures overlie the ridges and appear more intact. This superposition relationship potentially indicate that different stages of fracturing, compression, and sand venting may have occurred successively during the main shock and subsequent aftershocks.

Previous studies have shown that liquefaction-induced lateral spreading commonly causes the surface to break into large blocks, which then move, rotate, and collide under the combined action of gravity and seismic shaking (Youd, 1973, 2003). The deformation features observed in the Pengqu River valley and along the eastern shore of Dingmu Co Lake are consistent with this general pattern. In both areas, rear-edge extensional zones are developed upslope or toward the interior of the deformation body, whereas frontal compressional ridges occur toward the edge of the fan or floodplain. This geometric configuration indicates that rear-edge extension and frontal compression are kinematically linked expressions of the same spreading process. The exploratory comparison of morphometric parameters further supports this interpretation: extensional-zone width and compressional-ridge height vary positively among deformation units, suggesting that wider rear-edge extension is generally accompanied by stronger frontal shortening.

By contrast, the sand-volcano area does not show a stable statistical relationship with either extensional-zone width or compressional-ridge height. This indicates that the scale of sand venting is not controlled solely by the intensity of lateral spreading or frontal compression. Instead, it is more likely influenced by a combination of factors, including the local supply of liquefiable sand, the permeability structure of the shallow sediments, fracture connectivity, and the precise location of weak surface outlets. Therefore, sand venting should not be interpreted as

https://doi.org/10.5194/egusphere-2026-3290
Preprint. Discussion started: 24 August 2026

mechanically antagonistic to lateral spreading, but rather as an associated surface manifestation within the same liquefaction–deformation system, whose scale may vary independently from the bulk deformation geometry.

The deformation pattern in the Pengqu River floodplain is broadly similar to that on the eastern shore of Dingmu Co Lake, although the orientations differ. On the eastern shore of Dingmu Co Lake, the deformation units are mainly aligned parallel to the lakeshore, whereas along the Pengqu River they are aligned parallel to the river channel. This suggests that the geometry of the deformation units was strongly influenced by the local geomorphic boundary conditions. Despite these differences in orientation and scale, both areas display the same basic organization of rear-edge extension, frontal compression, and aligned sand venting, which supports the interpretation that they represent the same type of liquefaction-related lateral-spreading deformation unit developed in different sedimentary settings.

Based on these observations, we interpret the Dingri liquefaction deformation as a coupled process in which strong shaking first induced liquefaction of shallow sandy deposits, then triggered lateral spreading under the combined effects of gravity, local slope, and free-face conditions, and finally promoted sand venting along fractures and weak outlets within the deforming surface layer. In this framework, rear-edge extensional cracks, frontal compressional ridges, and frontal sand-volcano belts do not represent separate hazards, but different surface expressions of the same deformation system. This unit-based perspective is more consistent with the observed field relationships than a model based solely on isolated venting points or on a simple

https://doi.org/10.5194/egusphere-2026-3290
Preprint. Discussion started: 24 August 2026

negative correlation between sand venting and lateral spreading.

7.2 Implications for liquefaction hazards in the southern Tibetan Plateau

This study documents sand liquefaction triggered by a Mw 7.1 earthquake in the southern segment of the Shenza-Dingjie Rift Zone of the southern Tibetan Plateau. Previous studies have emphasized that the occurrence of sand liquefaction generally requires strong ground shaking, liquefiable sandy sediments, and shallow groundwater conditions (Housner, 1958; Ambraseys and Sarma, 1969; Iwasaki, 1986; Dobry, 1989; Ishihara, 1993; Zhong et al., 2023; Bol et al., 2024; Chen et al., 2024; Santiago et al., 2025). The Dingri earthquake provides a representative high-altitude case in which these three conditions coincided in river–lake margin environments under strong shaking.

The field evidence shows that the main liquefaction-prone materials in the study area include Holocene aeolian sands, fluvial sands, and ancient lacustrine sandy deposits (Li et al., 2025; Tie et al., 2025). These deposits are widely distributed not only within the Dingri earthquake area, but also across the southern Tibetan rift zone and other parts of the Tibetan Plateau (Pan et al., 2014; Gao et al., 2023). In addition, the region has experienced repeated strong earthquakes in historical time (Wu et al., 2015; Xu et al., 2025). Taken together, these conditions indicate that earthquake-induced liquefaction should be regarded as an important and probably under-recognized hazard in the southern Tibetan Plateau.

Previous studies have shown that the surface effects of liquefaction can include flow failures, lateral spreading, and rapid settlement (Seed, 1968; Youd, 1973,

https://doi.org/10.5194/egusphere-2026-3290
Preprint. Discussion started: 24 August 2026

2003; Bol et al., 2024; Chen et al., 2024; Santiago et al., 2025; Zhuang et al., 2025). The Dingri case shows that, in the plateau basin setting examined here, the dominant surface response was expressed mainly by lateral spreading accompanied by aligned sand venting, rather than by isolated settlement features. This indicates that hazard reconnaissance in similar high-altitude basins should not focus only on individual sand volcanoes, but should also pay attention to the broader deformation-unit structure, including rear-edge extensional cracks, frontal compressional ridges, and clusters of venting features.

The Dingri case also has broader methodological implications. In remote plateau environments, individual liquefaction manifestations are often discontinuous, short-lived, or difficult to access. A unit-based interpretation that combines field observations, UAV imagery, remote-sensing interpretation, and hydrogeologic constraints provides a more effective way to understand the organization of liquefaction-related deformation than point-based description alone. This approach may be particularly useful for rapid post-earthquake reconnaissance and for identifying areas where liquefaction-related lateral spreading is likely to pose a major hazard.

Accordingly, the broader significance of this study lies not only in documenting a new case of high-altitude liquefaction, but also in showing that liquefaction in plateau basins may be organized into recurrent lateral-spreading deformation units with internally coupled extensional, compressional, and venting features. This interpretation may help improve hazard identification and post-earthquake investigation in other tectonically active, sediment-filled basins of the Tibetan Plateau and comparable high-elevation regions.

7.3 Comparison with international liquefaction cases and broader implications

International liquefaction case histories have documented a wide range of surface deformation styles, from isolated sand boils and settlement to lateral spreading and catastrophic flow slides (Bhattacharya et al., 2011; Cetin et al., 2004; Sumer et al., 2002; Minarelli et al., 2022; Cetin et al., 2025; Bol et al., 2024). Within this spectrum, the Dingri case occupies a particular position. It is neither a typical urban liquefaction case dominated by building and lifeline damage, nor an extreme liquefaction-flow failure with long-runout movement. Instead, it represents a natural plateau-basin example in which liquefaction-related deformation is sufficiently preserved to reveal the internal organization of lateral-spreading units.

Classic cases such as the 1964 Niigata earthquake, the 1995 Kobe earthquake, and the 1999 Kocaeli earthquake have been fundamental in establishing the engineering significance of liquefaction. In these cases, sand boils, ground fissures, settlement, quay-wall displacement, and lateral spreading were closely linked to damage to buildings, bridges, port facilities, and other infrastructure (Bhattacharya et al., 2011; Cetin et al., 2004; Sumer et al., 2002). The main scientific and engineering focus of these studies was therefore on liquefaction susceptibility, foundation failure, lateral displacement, and damage mechanisms in urban, coastal, or reclaimed-ground settings. The Dingri case differs from these examples because the affected areas are

https://doi.org/10.5194/egusphere-2026-3290
Preprint. Discussion started: 24 August 2026

dominated by natural river–lake margin deposits and alluvial or floodplain surfaces rather than dense urban infrastructure or engineered coastal fills. As a result, the significance of the Dingri case does not lie primarily in structural damage analysis, but in the preservation and interpretation of natural liquefaction-related surface deformation.

A second group of international examples is represented by inventory-based studies in alluvial plains, such as the 2012 Emilia earthquake sequence and the 2023 Kahramanmaraş-Türkiye earthquake sequence. These studies have emphasized the systematic mapping of liquefaction points, soil ejecta, ground cracks, settlement, and lateral spreading, commonly supported by field surveys, remote-sensing interpretation, and geotechnical data (Minarelli et al., 2022; Cetin et al., 2025; Bol et al., 2024). The Dingri study follows this inventory-based tradition by identifying liquefaction points and mapping their spatial distribution. However, it also adds a second level of interpretation. Rather than treating liquefaction features only as individual points or isolated manifestations, this study groups repeated combinations of rear-edge extension, frontal compression, lateral spreading, and aligned sand venting into mappable deformation units. This unit-based perspective is the main methodological difference between the Dingri case and many conventional liquefaction inventories.

The 2010-2011 Canterbury earthquake sequence provides a closer methodological analogue because liquefaction and lateral spreading were mapped using field observations, aerial photographs, and remote-sensing data, particularly along rivers and floodplain environments (Cubrinovski et al., 2010, 2011, 2012). Both

https://doi.org/10.5194/egusphere-2026-3290
Preprint. Discussion started: 24 August 2026

Canterbury and Dingri demonstrate that image-based interpretation is particularly valuable where liquefaction features are spatially extensive and discontinuous. However, the emphasis of the two cases is different. Canterbury studies were strongly motivated by urban damage, repeated liquefaction, and lateral spreading impacts on residential areas and infrastructure. In contrast, the Dingri case is more useful for examining how liquefaction-related deformation is organized in a natural, high-altitude basin where direct engineering exposure is more limited but geomorphic evidence is well preserved. Therefore, Dingri complements Canterbury by showing how a similar field-image mapping strategy can be used to reconstruct deformation-unit geometry in a remote plateau environment.

At the other end of the deformation spectrum, the 2018 Palu-Donggala earthquake produced catastrophic liquefaction-related flow slides with very large horizontal displacement and severe destruction along the Palu Basin margin (Mason et al., 2021; Montgomery et al., 2021). The Dingri deformation is much smaller in scale and does not show evidence for long-runout liquefaction flow failure. Nevertheless, comparing Dingri with Palu is useful because both cases show that liquefaction-related ground failure may evolve beyond simple vertical sand venting. In Palu, this evolution reached the flow-slide end-member; in Dingri, it was expressed as organized lateral-spreading units with rear-edge extension, frontal shortening, and sand venting. Dingri may therefore be viewed as an intermediate case between isolated sand boils and large-scale liquefaction flow slides.

This comparison clarifies the specific contribution of the Dingri case. Existing

https://doi.org/10.5194/egusphere-2026-3290
Preprint. Discussion started: 24 August 2026

international studies have provided strong examples of liquefaction-induced engineering damage, coastal lateral spreading, alluvial-plain liquefaction inventories, and catastrophic flow slides. The Dingri earthquake adds a different type of case history: a natural high-altitude plateau-basin example in which the spatial coupling among extensional cracking, compressional ridging, lateral spreading, and sand venting can be observed within individual deformation units. This contribution is important because it shifts part of the interpretation from the occurrence of liquefaction features to their internal spatial organization.

Therefore, the Dingri case should be regarded as complementary to, rather than more severe than, the better-known international liquefaction examples. Its value lies in showing that earthquake-induced liquefaction in natural basin settings can be recorded not only by individual sand volcanoes or scattered ground cracks, but also by recurrent deformation units that preserve the kinematic relationship between rear-edge extension, frontal compression, and sand venting. This perspective may help bridge conventional point-based liquefaction inventories and broader interpretations of liquefaction-induced lateral spreading in remote sediment-filled basins.

8 Conclusion

Based on the above analysis, this study draws the following conclusions:

(1) The Dingri earthquake triggered widespread sand liquefaction in the Dingmu Co Basin, Guojia Basin, Dingjie Basin, and adjacent Pengqu River segments. In the main study area, the most prominent liquefaction-related surface damage was

https://doi.org/10.5194/egusphere-2026-3290
Preprint. Discussion started: 24 August 2026

expressed by lateral spreading, ground fissuring, compressional ridges, and sand venting, rather than by isolated liquefaction points alone.

(2) The observed cross-cutting and superposition relationships suggest a staged deformation process. Under the combined effects of strong shaking, gravity, and local geomorphic conditions, rear-edge tensile fractures first developed within the deforming ground. Liquefaction then caused sandy material to be expelled along fractures and weak outlets, while gentle slopes and free-face conditions promoted lateral spreading. During continued deformation, frontal compression formed compressional ridges, and in some locations new fractures developed near the frontal compressional zone, along which aligned sand venting occurred.

(3) The liquefaction-related deformation in the Dingri earthquake is best interpreted as a series of lateral-spreading deformation units composed of rear-edge extension, frontal compression, and aligned sand venting. The morphometric comparison shows that extensional-zone width and compressional-ridge height vary positively, indicating that rear-edge extension and frontal shortening are kinematically linked expressions of the same spreading process. In contrast, sand-volcano area does not show a stable statistical relationship with these two deformation parameters, suggesting that sand venting is an associated surface manifestation within the same liquefaction–deformation system, but its scale is additionally influenced by local sediment supply, permeability structure, fracture connectivity, and surface outlet conditions.

(4) The Dingri case demonstrates that earthquake-induced liquefaction in high-altitude plateau basins may be organized into recurrent deformation units rather than isolated vents. Therefore, pre-earthquake hazard assessment and post-earthquake reconnaissance in the southern Tibetan Rift Zone and across the Tibetan Plateau should pay particular attention not only to individual sand volcanoes, but also to rear-edge extensional cracks, frontal compressional ridges, and other indicators of liquefaction-related lateral spreading, so as to improve post-earthquake reconnaissance and liquefaction hazard identification.

Reference

Ambraseys, N. N. and Sarma, S. K.: Liquefaction of soils induced by earthquakes, Bull. Seismol. Soc. Am., 59, 651–664, https://doi.org/10.1785/BSSA0590020651, 1969.

Bhattacharya, S., Hyodo, M., Goda, K., Tazoh, T., and Taylor, C. A.: Liquefaction of soil in the Tokyo Bay area from the 2011 Tohoku (Japan) earthquake, Soil Dyn. Earthq. Eng., 31, 1618–1628, https://doi.org/10.1016/j.soildyn.2011.06.006, 2011.

Bol, E., Özocak, A., Sert, S., Çetin, K. Ö., Arslan, E., Kocaman, K., and Ayhan, B. U.: Evaluation of soil liquefaction in the city of Hatay triggered after the February 6, 2023 Kahramanmaraş–Türkiye earthquake sequence, Eng. Geol., 339, 107648, https://doi.org/10.1016/j.enggeo.2024.107648, 2024.

https://doi.org/10.5194/egusphere-2026-3290
Preprint. Discussion started: 24 August 2026

Cetin, K. O., Youd, T. L., Seed, R. B., Bray, J. D., Stewart, J. P., Durgunoglu, H. T., Lettis, W., and Yilmaz, M. T.: Liquefaction-induced lateral spreading at Izmit Bay during the 1999 Kocaeli (Izmit)–Turkey earthquake, J. Geotech. Geoenviron. Eng., 130, 1300–1313, https://doi.org/10.1061/(ASCE)1090-0241(2004)130:12(1300), 2004.

Cetin, K. O., Soylemez, B., Guzel, H., and Cakir, E.: Soil liquefaction sites following the February 6, 2023, Kahramanmaraş–Türkiye earthquake sequence, Bull. Earthq. Eng., 23, 921–944, https://doi.org/10.1007/s10518-024-01875-3, 2025.

Chen, L., Lei, J., and Wang, Y.: Liquefaction phenomena following the February 6th, 2023, Turkiye earthquakes: observation and lessons, Nat. Hazards, 120, 10709–10726, https://doi.org/10.1007/s11069-024-06623-z, 2024.

Cubrinovski, M. and Green, R. A. (Eds.): Geotechnical reconnaissance of the 2010 Darfield (Canterbury) earthquake, GEER Association Report, 2010.

Cubrinovski, M., Bradley, B., Wotherspoon, L., Green, R., Bray, J., Wood, C., Pender, M., Allen, J., Bradshaw, A., Rix, G., Taylor, M., Robinson, K., Henderson, D., Giorgini, S., Ma, K., Winkley, A., Zupan, J., O'Rourke, T., DePascale, G., and Wells, D.: Geotechnical aspects of the 22 February 2011 Christchurch earthquake, Bull. N. Z. Soc. Earthq. Eng., 44, 205–226, https://doi.org/10.5459/bnzsee.44.4.205-226, 2011.

Cubrinovski, M., Robinson, K., Taylor, M., Hughes, M., and Orense, R.: Lateral spreading and its impacts in urban areas in the 2010–2011 Christchurch earthquakes,

https://doi.org/10.5194/egusphere-2026-3290
Preprint. Discussion started: 24 August 2026

N. Z. J. Geol. Geophys., 55, 255–269, https://doi.org/10.1080/00288306.2012.699895, 2012.

Dobry, R.: Some basic aspects of soil liquefaction during earthquakes, Ann. N. Y. Acad. Sci., 558, 172–182, https://doi.org/10.1111/j.1749-6632.1989.tb22567.x, 1989.

Gao, Y., Li, M., Wu, Z. H., Zhang, K. Q., Zuo, J. M., Tian, T. T., and Wang, S. F.: Late Quaternary normal faulting along the western boundary fault of Peiku Co graben in southern Nyalam–Coqen rift: implications for extensional deformation in southern Tibet and seismic hazard, J. Struct. Geol., 181, 105087, https://doi.org/10.1016/j.jsg.2024.105087, 2024.

Rathje, E. M. and Franke, K. W.: Remote sensing for geotechnical earthquake reconnaissance, Soil Dyn. Earthq. Eng., 91, 304–316, https://doi. org/10. 1016/j. soildyn. 2016.09.016, 2016.

Gao, Y., Zhang, K., Wu, Z., Tian, T., and Li, B.: Factors controlling the Early–Mid Holocene aeolian sediment accumulation in the Pum Qu catchment and environmental implications for the southern Tibetan Plateau, Quat. Int., 652, 17–32, https://doi.org/10.1016/j.quaint.2022.11.008, 2023.

Ha, I. S., Olson, S. M., Seo, M. W., and Kim, M. M.: Evaluation of reliquefaction resistance using shaking table tests, Soil Dyn. Earthq. Eng., 31, 682–691, https://doi.org/10.1016/j.soildyn.2010.12.008, 2011.

https://doi.org/10.5194/egusphere-2026-3290
Preprint. Discussion started: 24 August 2026

Hou, L. Y., Shan, X. J., Gong, W. Y., Zhang, Y. F., Luo, H., and Zhao, D. Z.: Research on the characteristics of the 2016 Dingjie earthquake sequence based on multi-period DInSAR data, Chinese J. Geophys., 63, 1357–1369, 2020.

Housner, G. W.: The mechanism of sandblows, Bull. Seismol. Soc. Am., 48, 155–161, 1958.

Huang, Y. and Yu, M.: Review of soil liquefaction characteristics during major earthquakes of the twenty-first century, Nat. Hazards, 65, 2375–2384, https://doi.org/10.1007/s11069-012-0433-9, 2013.

Ishihara, K.: Liquefaction and flow failure during earthquakes, Géotechnique, 43, 351–415, 1993.

Iwasaki, T.: Soil liquefaction studies in Japan: state-of-the-art, Soil Dyn. Earthq. Eng., 5, 2–68, 1986.

Jin, W. X.: Debris flow risk assessment of Daduogou, Dingri County, Tibet, Chengdu University of Technology, 2019.

Li, Z. C., Wu, Z. H., Han, S., Gao, Y., Huang, T., Fan, F. X., Tian, T. T., and Lu, S. M.: Characteristics and mechanisms of sand liquefaction in the MS6.8 Dingri earthquake on January 7, 2025, Earth Sci., 50, 1830–1841, 2025.

https://doi.org/10.5194/egusphere-2026-3290
Preprint. Discussion started: 24 August 2026

Liu, C. Z., Liang, K., and Wang, X. Y.: Analysis of the causality of the Dashagou debris flow disaster chain in the Ms 6.2 earthquake area of Jishishan, Geol. Rev., 70, 960–974, https://doi.org/10.16509/j.georeview.2024.04.011, 2024.

Liu, F. C., Pan, J. W., Li, H. B., Yang, S. H., Wu, K. G., Su, Q., Zhang, S. Q., Chevalier, M. L., and Lu, H. J.: Surface rupture and coseismic displacement distribution of the Mw7.1 Dingri, Tibet earthquake in 2025, Acta Geol. Sin., 99, 685–703, https://doi.org/10.19762/j.cnki.dizhixuebao.2025069, 2025.

Liu, Z. J., Wang, P., Zhang, Z., Li, Z. G., Cao, Z. Z., Zhang, J. Z., Yuan, X. M., Wang, W., and Xing, X. C.: Liquefaction in western Sichuan Basin during the 2008 Mw 7.9 Wenchuan earthquake, China, Tectonophysics, 694, 214–238, https://doi.org/10.1016/j.tecto.2016.11.005, 2017.

Mason, H. B., Montgomery, J., Gallant, A. P., Hutabarat, D., Reed, A. N., Wartman, J., Irsyam, M., Simatupang, P. T., Alatas, I. M., Prakoso, W. A., Djarwadi, D., Hanifa, R., Rahardjo, P., Faizal, L., Harnanto, D. S., Kawanda, A., Himawan, A., and Yasin, W.: East Palu Valley flowslides induced by the 2018 Mw 7.5 Palu-Donggala earthquake, Geomorphology, 373, 107482, https://doi.org/10.1016/j.geomorph.2020.107482, 2021.

Minarelli, L., Amoroso, S., Tarabusi, G., Stefani, M., and Pulelli, G.: Liquefied sites of the 2012 Emilia earthquake: a comprehensive database of the geological and geotechnical features, Bull. Earthq. Eng., 20, 3057–3091, 2022.

https://doi.org/10.5194/egusphere-2026-3290
Preprint. Discussion started: 24 August 2026

Montgomery, J., et al.: Field reconnaissance data from GEER investigation of the 2018 Palu-Donggala earthquake, Data Brief, 34, 106682, 2021.

Pan, M., Wu, Y., Zheng, Y., and Tan, L.: Holocene aeolian activity in the Dinggye area (southern Tibet, China), Aeolian Res., 12, 19–27, https://doi.org/10.1016/j.aeolia.2013.11.002, 2014.

Ren, Y. F., Wang, H. W., Diao, H. Q., Liu, Y., Qiang, S. Y., Zhou, B. F., and Wen, R. Z.: Rapid generation and sharing of strong-motion time histories on a 2025-km grid: a case study of the MS 6.8 Dingri, Tibet earthquake on January 7, 2025, Earthq. Eng. Eng. Vib., 45, 1–11, 2025.

Santiago, Y., Ledezma, C., and Tiznado, J. C.: Assessing soil liquefaction due to large-magnitude subduction earthquakes, Soil Dyn. Earthq. Eng., 188, 109069, https://doi.org/10.1016/j.soildyn.2024.109069, 2025.

Seed, B.: Landslides during earthquakes due to liquefaction, J. Soil Mech. Found. Div., 94, 1053–1122, 1968.

Shao, Y. X., Wang, A. S., Liu, J., Wang, W. X., Han, L. F., Xing, L. Y., Xu, J. H., Wang, J. C., Yao, W. Q., Zhang, H. X., and Liu, X. L.: Preliminary results of surface rupture characteristics and field coseismic displacement measurements of the January 7, 2025 Dingri, Tibet earthquake, Earth Sci., 1–28, 2025.

https://doi.org/10.5194/egusphere-2026-3290
Preprint. Discussion started: 24 August 2026

Sumer, B. M., Hatipoglu, F., Fredsøe, J., and Sumer, S. K.: Impact of liquefaction on coastal structures in the 1999 Kocaeli, Turkey earthquake, Soil Dyn. Earthq. Eng., 22, 975–984, 2002.

Tian, T. T. and Wu, Z. H.: The latest prehistoric large earthquake events of the Dingmu Co normal fault in the southern segment of the Shenzha-Dingjie rift, Tibet, and their seismogeological significance, Geol. Rev., 69, 53–55, https://doi.org/10.16509/j.georeview.2023.s1.020, 2023.

Tie, Y. B., Gao, Y. J., Zhang, X. Z., Shi, A. W., Huang, W. J., Qing, Y. E., Li, Z. L., Dong, L., and Ning, Z. J.: Study on geological disaster development and mitigation in the Ms 6.8 earthquake area of Dingri County, Tibet, Sediment. Tethyan Geol., 1–20, https://doi.org/10.19826/j.cnki.1009-3850.2025.01002, 2025.

Wang, W., Liu-Zeng, J., Shao, Y., Wang, Z., Han, L., Shen, X., Qin, K., Gao, Y., Yao, W., Hu, G., Zeng, X., Liu, X., Wang, W., Cui, F., Liu, Z., Li, J., and Tu, H.: Mapping of soil liquefaction associated with the 2021 Mw 7.4 Maduo (Madoi) earthquake based on the UAV photogrammetry technology, Remote Sens., 15, 1032, https://doi.org/10.3390/rs15041032, 2023.

Wu, Z. H., Ye, P. S., Wang, C. M., Zhang, K. Q., Zhao, H., Zheng, Y. G., Yin, J. H., and Li, H. H.: Prehistoric earthquake relics, age and geological significance of the Angang graben in southern Tibet, Earth Sci., 40, 1621–1642, 2015.

https://doi.org/10.5194/egusphere-2026-3290
Preprint. Discussion started: 24 August 2026

Xia, P., Zhou, Y. G., Chen, Y. M., and Gao, Y. F.: Liquefaction evaluation on sand-like gravelly soil deposits based on field Vs measurements during the 2008 Wenchuan earthquake, Eng. Geol., 343, 107782, https://doi.org/10.1016/j.enggeo.2024.107782, 2024.

Xu, Y. R., Dou, A. X., Li, Z. M., Liang, P., Liang, Z. L., and Lu, L. Y.: A rapid assessment of the secondary disasters triggered by the December 18, 2023 Ms 6.2 earthquake in Jishishan, Gansu, Earthquake, 44, 209–215, 2024.

Xu, Y. R., Fu, G. C., Liang, Z. Y., Hu, G. M., Zhou, X. C., Shi, F., and Yao, Y.: Preliminary study on the characteristics of landslides and sand liquefaction induced by the January 7, 2025 Ms 6.8 earthquake in Dingri, Tibet, Earth Sci., 1–26, 2025.

Yao, J., Yao, D., Chen, F., Zhi, M., Sun, L., and Wang, D.: A preliminary catalog of early aftershocks following the 7 January 2025 Ms 6.8 Dingri, Xizang earthquake, J. Earth Sci., 1–5, https://doi.org/10.1007/s12583-025-2020-x, 2025.

Yao, X., Zhang, J. G., Zhang, Y. S., Yang, B., and Yu, K.: Research on the characteristics of sand liquefaction disasters induced by the March 10, 2011 Yijing 5.8 earthquake, J. Eng. Geol., 19, 152–161, 2011.

Youd, T. L.: Liquefaction mechanisms and induced ground failure, Int. Geophys., 81, 1159–1173, 2003.

https://doi.org/10.5194/egusphere-2026-3290
Preprint. Discussion started: 24 August 2026

Youd, T. L.: Liquefaction, flow, and associated ground failure, U.S. Geol. Surv. Circ., 832, 1973.

Zhang, X. T., Jiang, X. H., Xue, Y., Yao, Q., Jie, M. Y., Zang, Y., Song, J., Lu, X., Yu, C., Yuan, Z. Y., and Tian, L.: Summary of the March 20, 2020 Ms 5.9 earthquake in Dingri, Tibet, Seismol. Geomagn. Obs. Res., 41, 193–203, 2020.

Zhong, J. H., Ni, L. T., Sun, N. L., et al.: An unusual widespread liquefaction caused by a magnitude 5.1 earthquake: activation effect of salt dissolution on sand gravel liquefaction and its mechanism, Geol. Rev., 69, 1543–1563, 2023.

Zhuang, H. Y., Li, X. X., Zhao, K., Wang, S. L., Li, Z. Y., and Chen, G. X.: Liquefaction-induced lateral spreading characteristics of the fluvial terraces at the lower reaches of Yangtze River, Eng. Geol., 346, 107900, https://doi.org/10.1016/j.enggeo.2024.107900, 2025.

Data availability

All relevant data supporting the findings of this study are available in the Mendeley Data repository. This includes the seismic catalog data and the characteristics of deformation zones derived from field investigations and remote sensing interpretation. The dataset can be accessed via the persistent identifier (DOI): [10.17632/dt5m8tjkcs.1].

Author Contributions:

https://doi.org/10.5194/egusphere-2026-3290
Preprint. Discussion started: 24 August 2026

Zhichao Li: Conceptualization, field investigation, data analysis, and manuscript drafting. **Zhonghai Wu**: Supervision, methodology development, and final manuscript review. **Shuai Han:** Investigation, data curation, and figure preparation. **Yang Gao**: Figure preparation, Conceptualization. **Ting Huang**: Field investigation, interpretation. **Fuxin Fan**: Field investigation, Drone data acquisition.**Tingting Tian:** Field investigation. **Shiming Lu:** Provision of remote sensing imagery.

Competing interests

The authors declare that there are no conflicts of interest regarding the publication of this article.

Acknowledgments

We gratefully acknowledge the Institute of Geophysics, China Earthquake Administration, and China Railway First Survey and Design Institute Group Co., Ltd. for providing the Dingri borehole data; Professor Wang Dun of China University of Geosciences (Wuhan) for the precise aftershock relocation data; and Researcher Ruizhi Wen of the Institute of Engineering Mechanics, China Earthquake Administration, for the D0007 observational data.

Financial support

This work was supported by National Natural Science Foundation of China (42472287, 42402229).

https://doi.org/10.5194/egusphere-2026-3290
Preprint. Discussion started: 24 August 2026

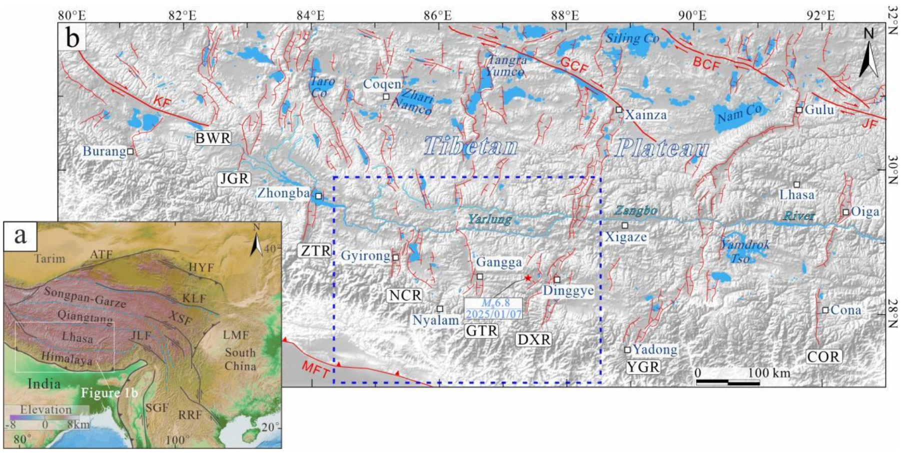

Figure 1. Tectonic location of the seismic area and distribution of the southern Tibet rifts (Figure 1b is from Gao et al., 2024). COR: Cuona-Woka Rift, YGR: Yadong-Gulu Rift, DXR: Dingjie-Shenzen Rift, GTR: Gangga-Dangra Yumco Rift, NCR: Nyalam-Cuoqin Rift, ZTR: Zhongba-Taruo Co Rift, JGR: Jiangqu Zangbu-Gaize Rift, BWR: Pulan-Wenbu Dangxiong Rift, GCR: Geren Co Fault, BCR: Bencuo Fault, KF: Karakoram Fault, XF: Xianshuihe Fault, JF: Jiali Fault, ATF: Altyn Tagh Fault, MFT: Main Frontal Thrust.

https://doi.org/10.5194/egusphere-2026-3290
Preprint. Discussion started: 24 August 2026

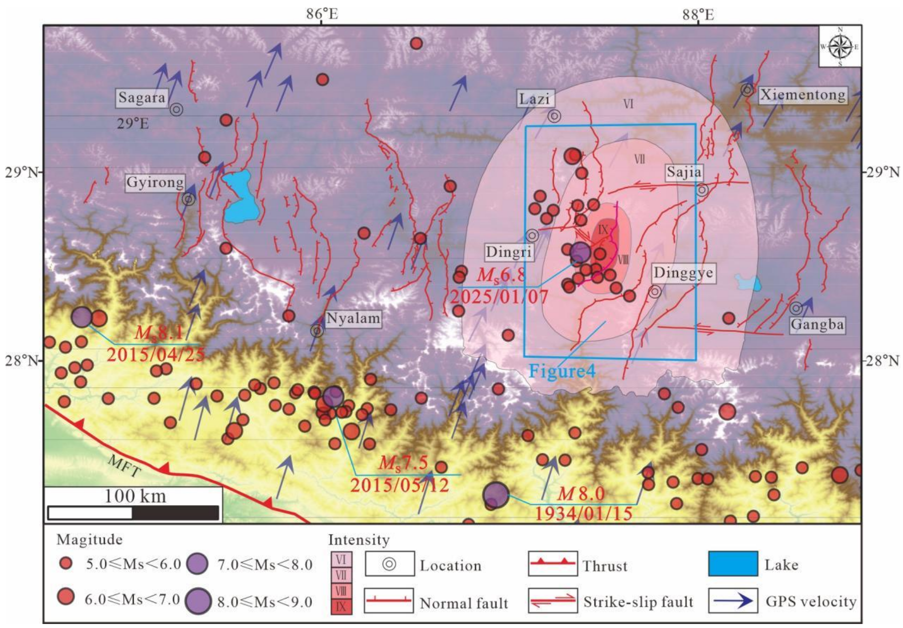

Figure 2. Seismicity Distribution Map of Shigatse and Its Neighboring Areas.

https://doi.org/10.5194/egusphere-2026-3290
Preprint. Discussion started: 24 August 2026

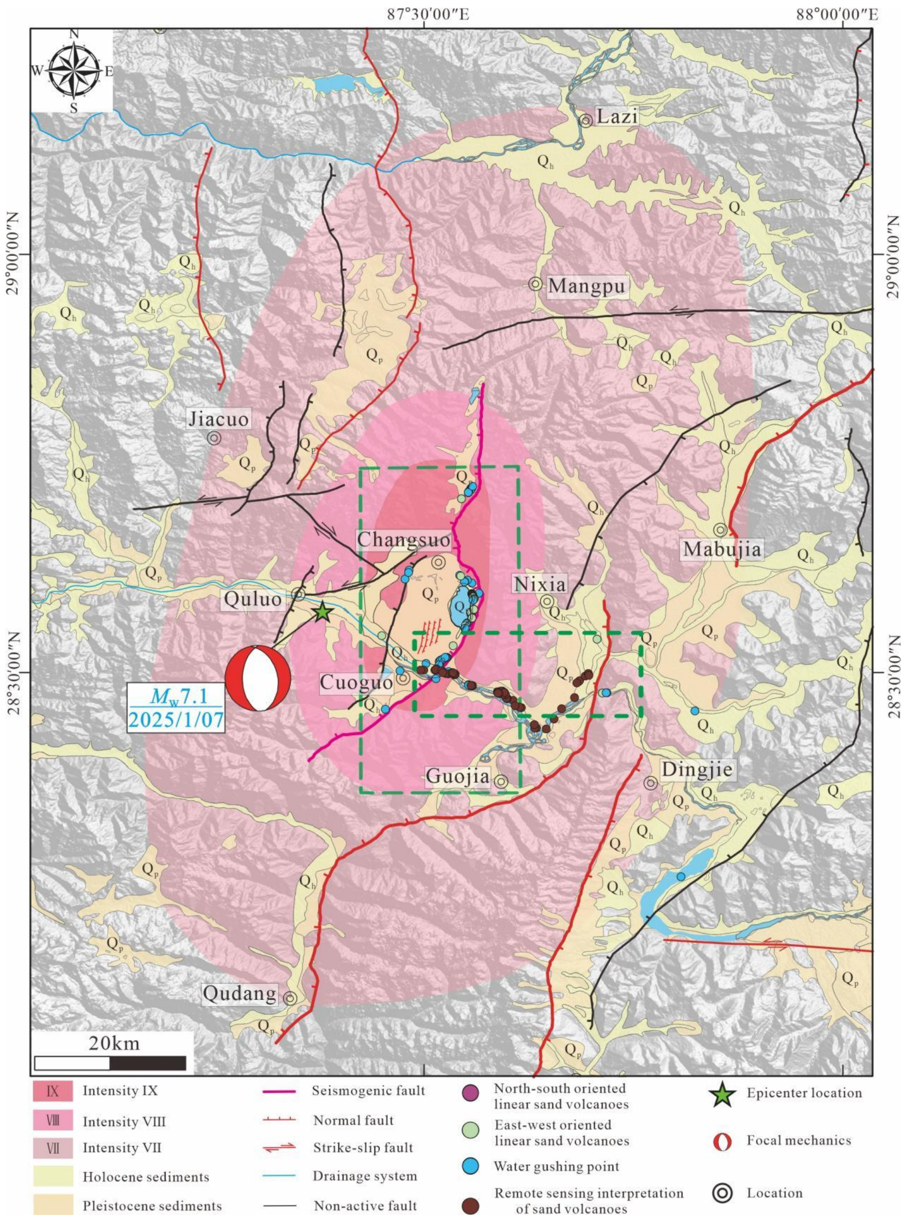

Figure 3.Distribution map of sand gushing and water spouting during the Dingri earthquake（The epicenter location is from the U.S. Geological Survey）

https://doi.org/10.5194/egusphere-2026-3290
Preprint. Discussion started: 24 August 2026

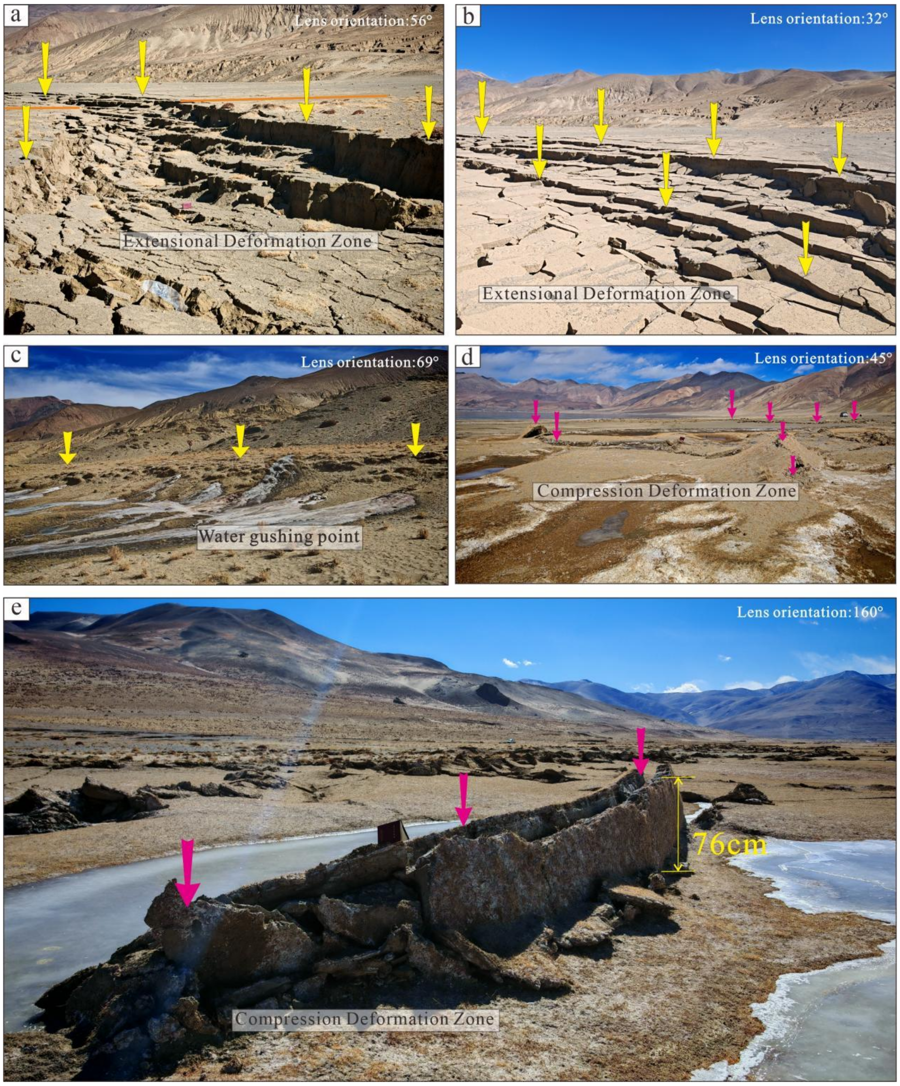

Figure 4. Schematic diagram of surface deformation characteristics and field photos of the Dingri earthquake. a, b. Extensional deformation at the eastern rear edge of Dingmu Co Lake; c. Springs developed on the steep scarp of the old fault; d, e. Compressional deformation at the eastern front edge of Dingmu Co Lake.

https://doi.org/10.5194/egusphere-2026-3290
Preprint. Discussion started: 24 August 2026

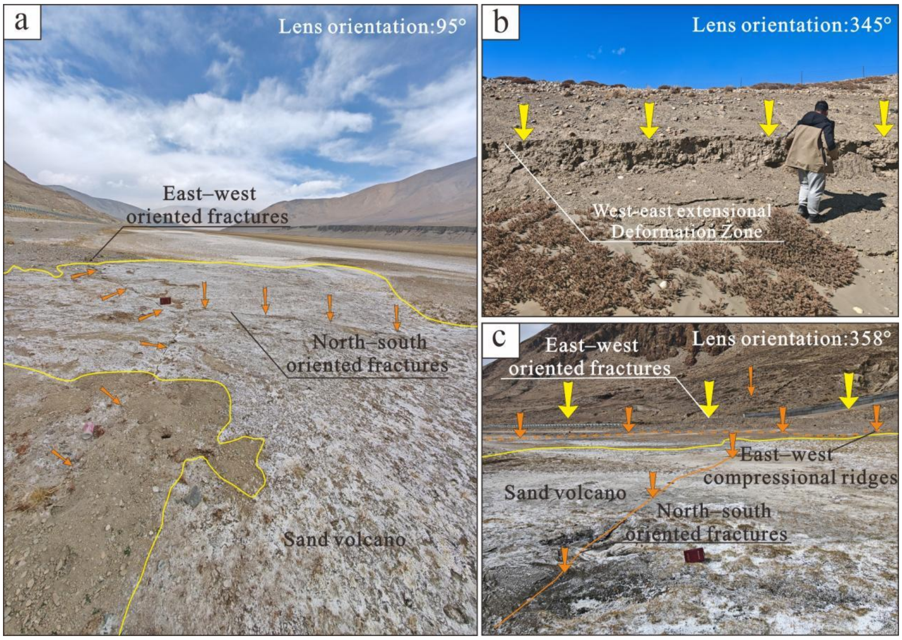

Figure 5. Liquefaction deformation characteristics of the Pengqu Riverbank. a. Sand volcanoes developed on the bed of the Pengqu River; b. Extensional deformation at the rear edge of the Pengqu River bed; c. The relationship between compressional ridges and sand volcanoes in the Pengqu River bed.

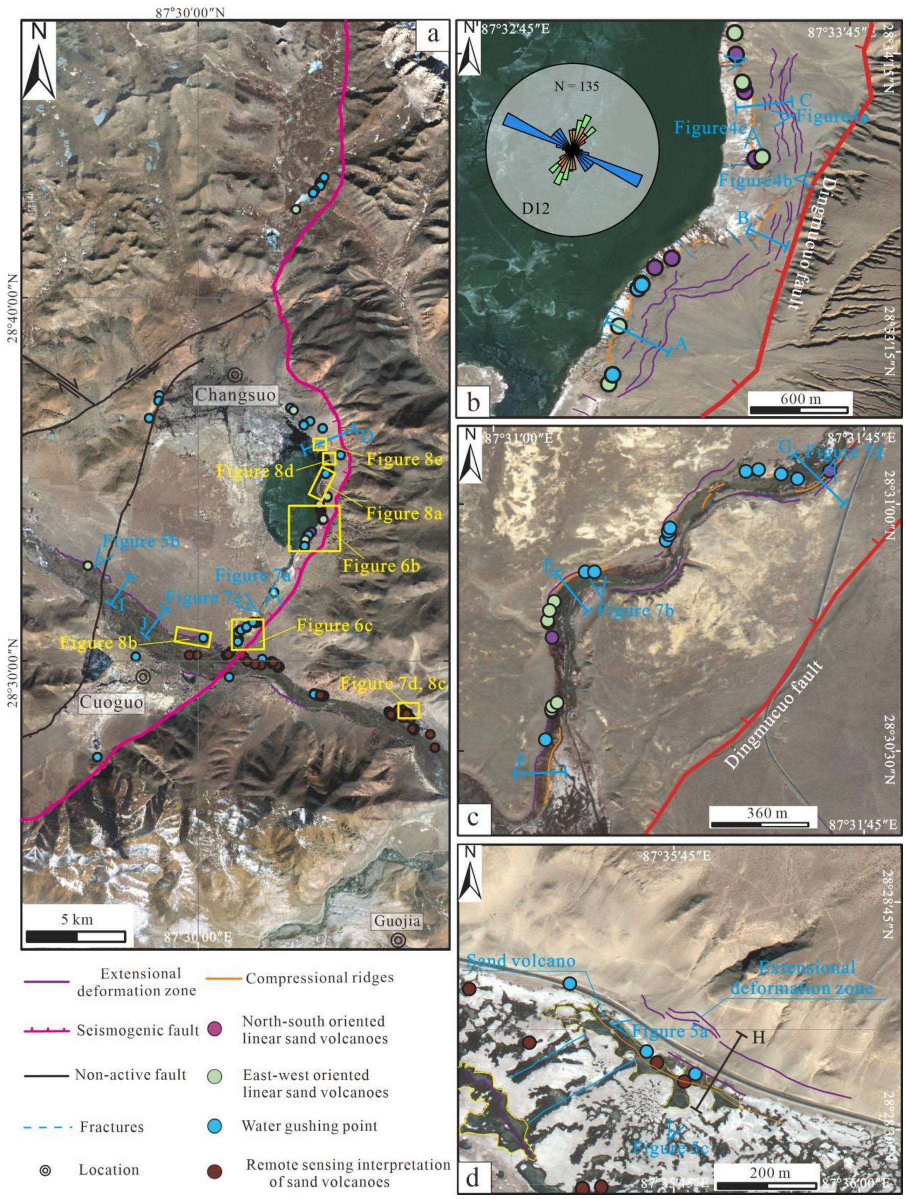

Figure 6. Post-earthquake remote sensing images (Data from 91 Weitu: https: //www. 91weitu. com/). a. Overall distribution of liquefaction points in sandy soil; b. Post-earthquake remote sensing image of the eastern part of Dingmu Co Lake (survey area D12); c. Post-earthquake remote sensing image of the southern part of Dingmu Co Lake; d. Post-earthquake remote sensing image of the northern bank of the Pengqu River.

https://doi.org/10.5194/egusphere-2026-3290
Preprint. Discussion started: 24 August 2026

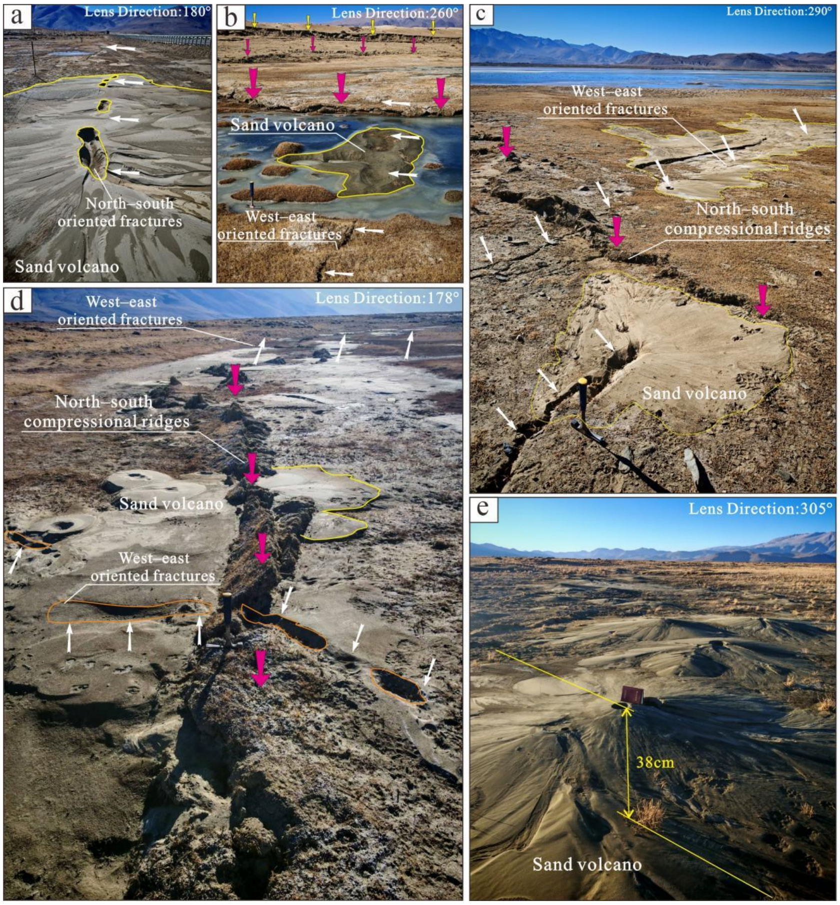

Figure 7. Characteristics of liquefaction sand volcanoes in the Dingri earthquake. a. Sand volcanoes on the eastern side of the Gading Line; b. East-west oriented liquefaction sand volcanoes developed in the river valley on the western side of the Gading Line; c. East-west oriented liquefaction sand volcanoes on the northeastern shore of Dingmu Co Lake; d. East-west and north-south oriented fissures developed in the river valley on the western side of the Gading Line, accompanied by sand volcanoes; e. Sand volcanoes developed in the Pengqu River Valley.

https://doi.org/10.5194/egusphere-2026-3290
Preprint. Discussion started: 24 August 2026

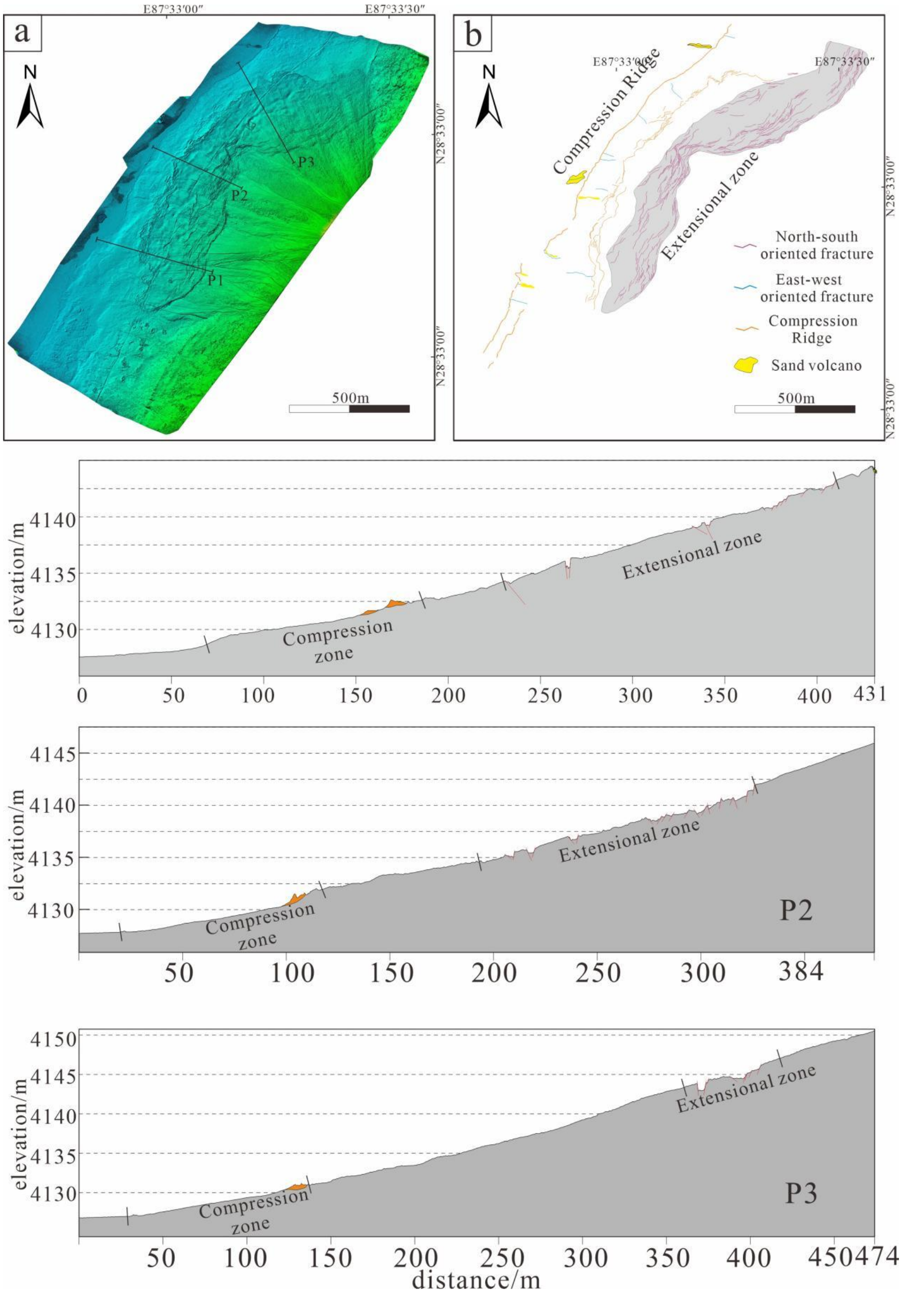

Figure 8. a. Post-earthquake DEM derived from UAV imagery. b. DEM interpretation showing elevation profiles P1, P2, and P3.

https://doi.org/10.5194/egusphere-2026-3290
Preprint. Discussion started: 24 August 2026

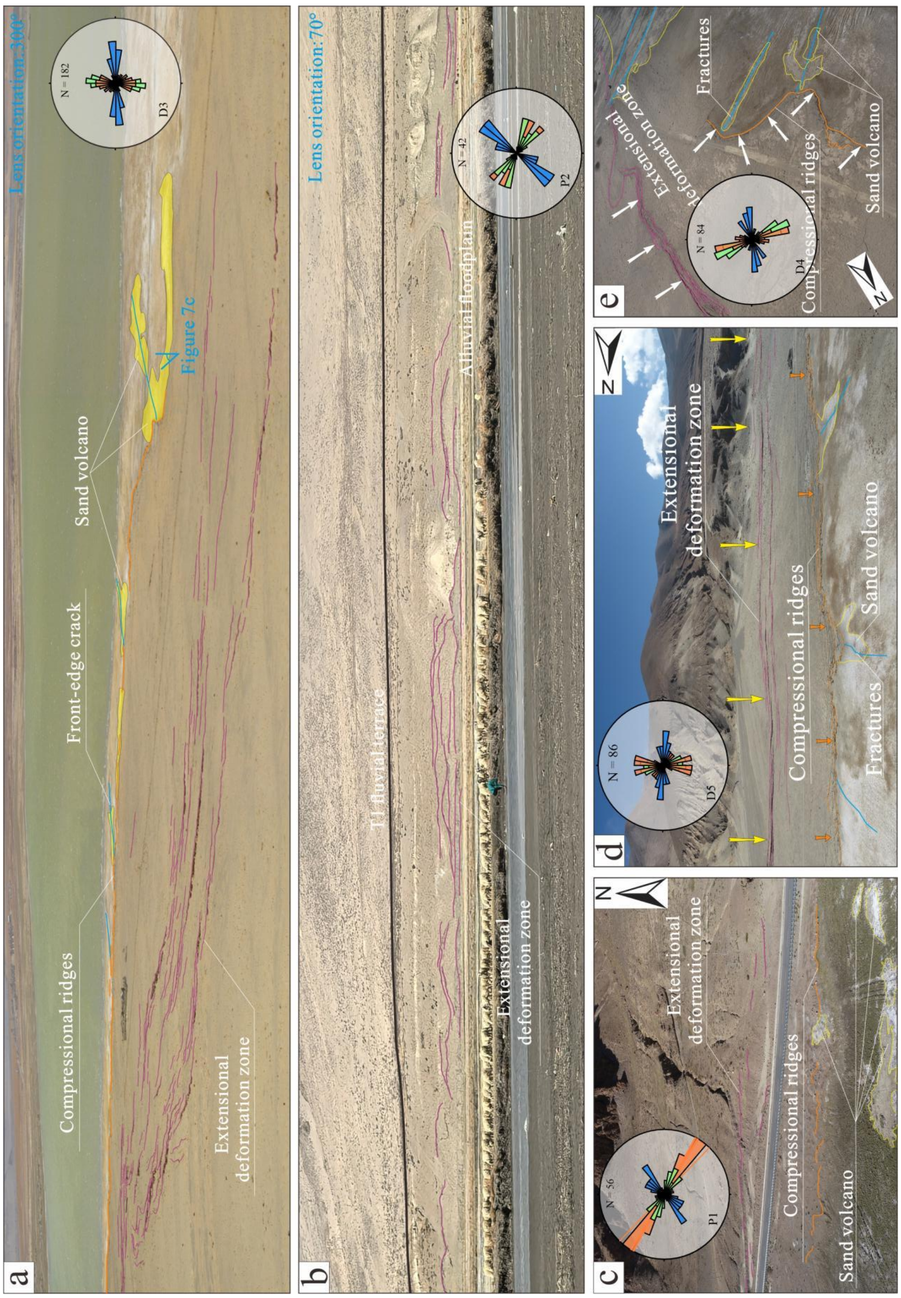

https://doi.org/10.5194/egusphere-2026-3290
Preprint. Discussion started: 24 August 2026

Figure 9. Characteristics of the extensional deformation zone. a. Macroscopic view of liquefaction deformation features east of Dingmu Co Lake (survey area D3); b. Liquefaction deformation features on the Pengqu River bank (survey area P2); c. Liquefaction deformation features on the Pengqu River bank (survey area P1; photo taken by UAV aerial photography); d. Liquefaction deformation features east of Dingmu Co Lake (survey area D5; photo taken by UAV aerial photography); e. Liquefaction deformation features east of Dingmu Co Lake (survey area D4; photo taken by UAV aerial photography).

https://doi.org/10.5194/egusphere-2026-3290
Preprint. Discussion started: 24 August 2026

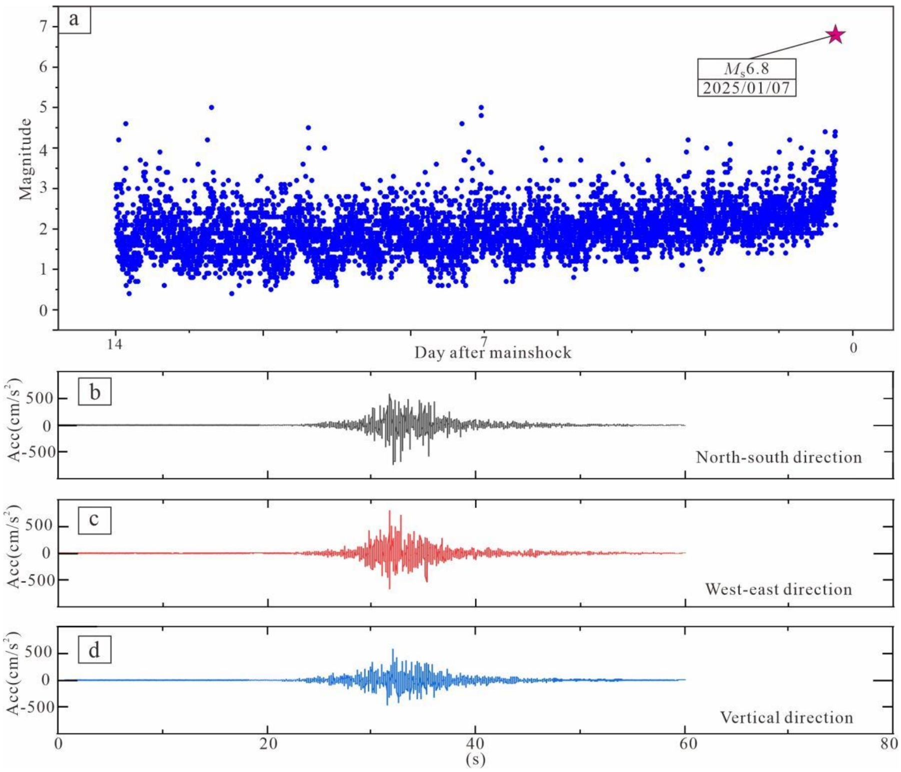

Figure 10. a. Distribution of aftershocks within two weeks after the earthquake (Yao et al., 2025); b. North-South (NS) Directional Seismic Ground Motion Accelerationrecorded by D0007; c. West-East (WE) Directional Seismic Ground Motion Accelerationrecorded by D0007; d. Vertical Directional Seismic Ground Motion Accelerationrecorded by D0007 (D0007 data from Ren et al., 2025).

https://doi.org/10.5194/egusphere-2026-3290
Preprint. Discussion started: 24 August 2026

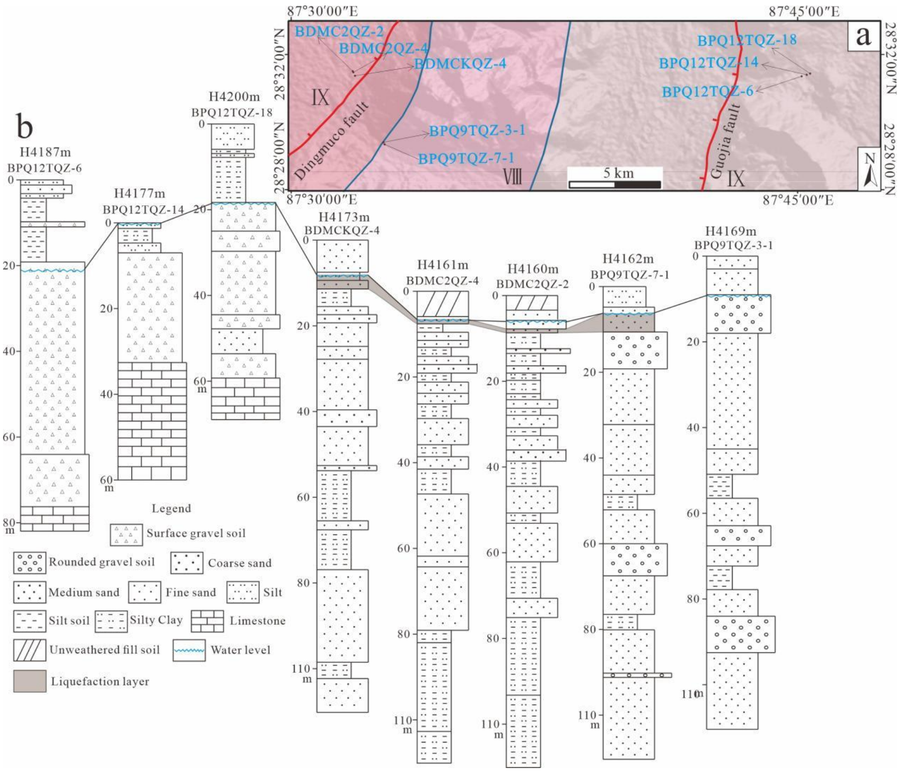

Figure 11. Borehole section map of the earthquake-affected area. a. Borehole spatial distribution map; b. Borehole columnar diagram.

https://doi.org/10.5194/egusphere-2026-3290
Preprint. Discussion started: 24 August 2026

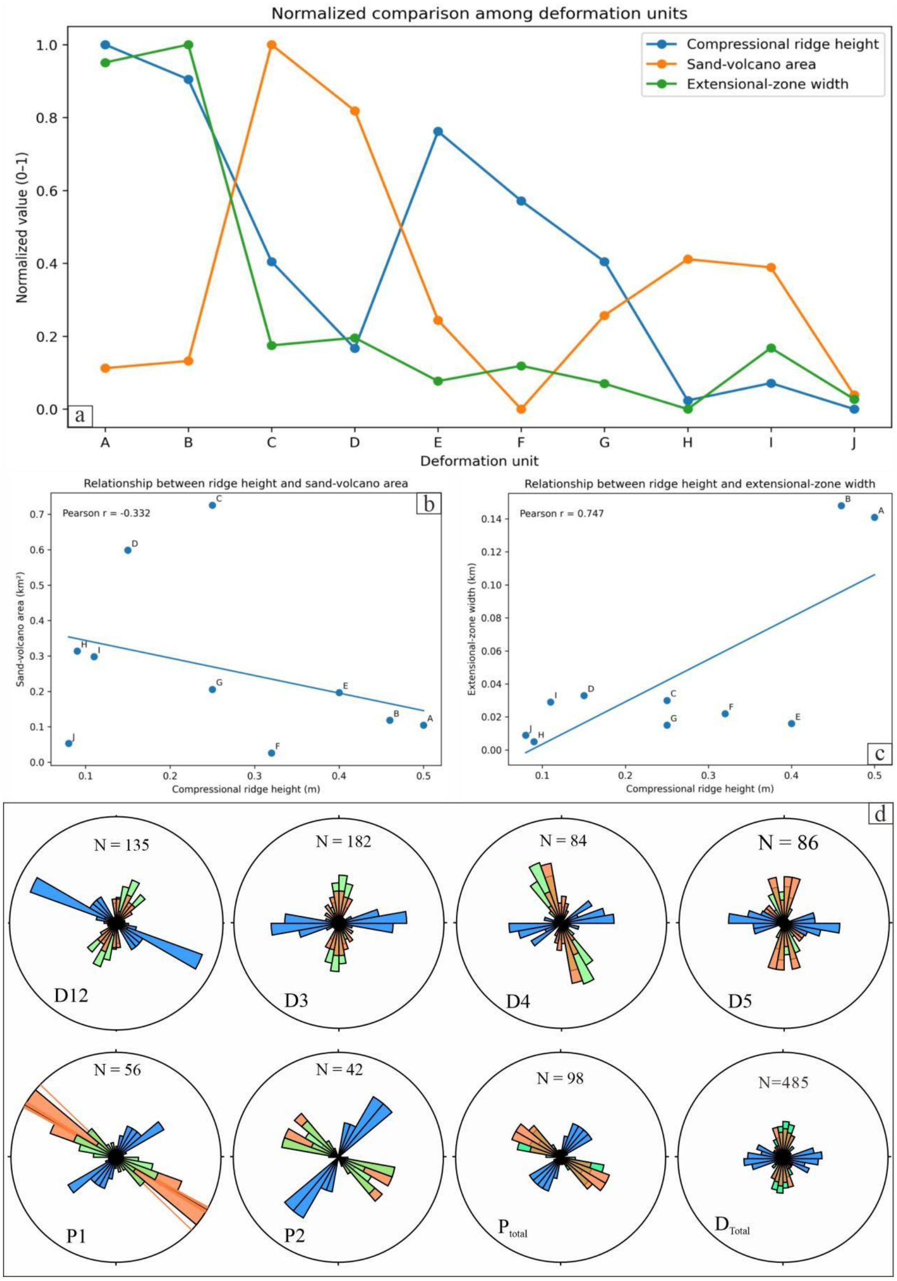

Figure 12. a. Normalized values of compressional-ridge height, sand-volcano area, and extensional-zone width for ten representative deformation units. The normalization was used only for visual comparison among parameters with different dimensions. b. Scatter plot showing the relationship between compressional-ridge height and apparent sand-volcano area. The weak negative correlation suggests that sand-venting area is not simply controlled by the magnitude of frontal compression. c.

https://doi.org/10.5194/egusphere-2026-3290
Preprint. Discussion started: 24 August 2026

Scatter plot showing the relationship between compressional-ridge height and extensional-zone width. The positive correlation is consistent with the interpretation that rear-edge extension and frontal compression are mechanically linked during lateral spreading. d. Green represents the dominant orientation of tension fractures generated by rear edge horizontal expansion, blue represents the dominant orientation of tension fractures associated with sand volcano development at the front edge, and yellow represents the dominant at the front edge.

https://doi.org/10.5194/egusphere-2026-3290
Preprint. Discussion started: 24 August 2026

1018 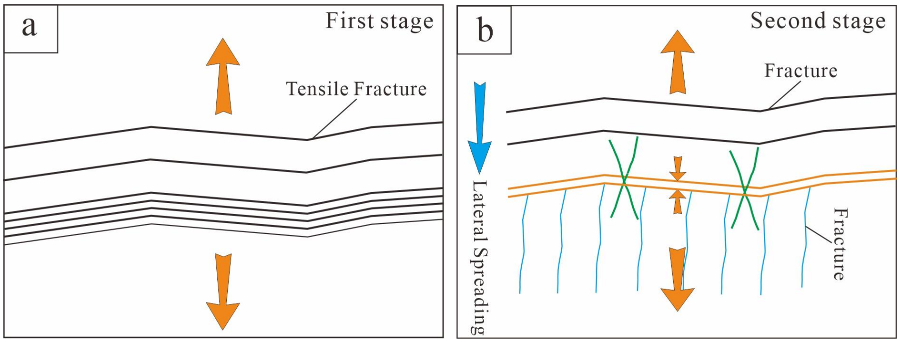

1019 Figure 13. Schematic illustration of the regional stress field. a. After an earthquake,
1020 tensional cracks are generated; b. As liquefaction progresses, compressional ridges,
1021 shear fractures, and sand volcanoes are generated.

1022

https://doi.org/10.5194/egusphere-2026-3290
Preprint. Discussion started: 24 August 2026

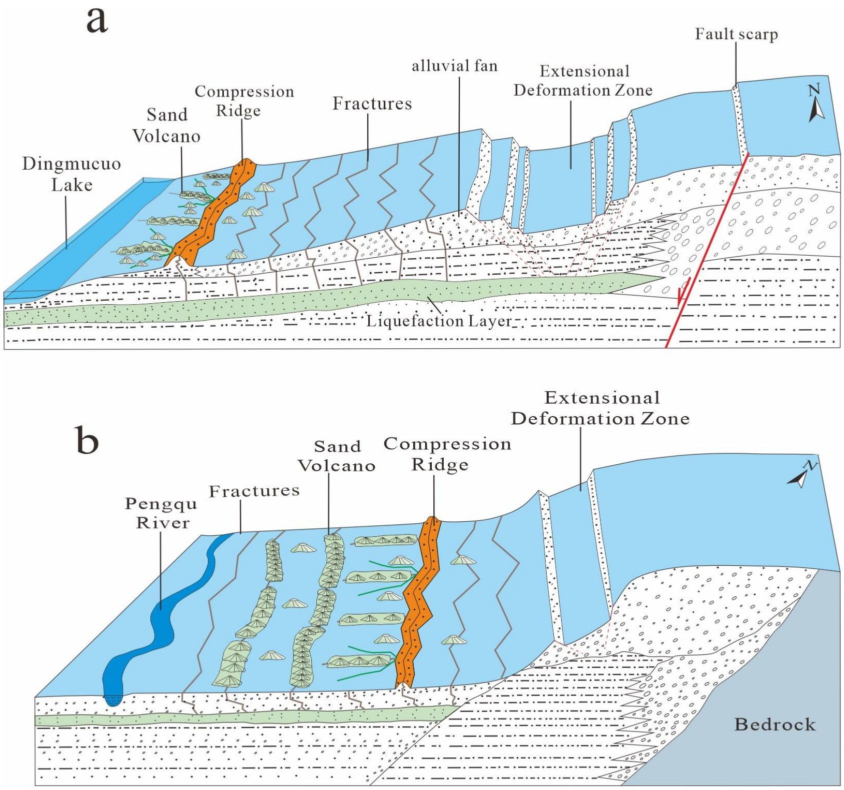

Figure 14. Different surface deformation patterns on the eastern shore of Dingmu Co Lake and the Pengqu River. a. Liquefaction deformation pattern east of Dingmu Co Lake; b. Deformation pattern of the Pengqu River.